

DHIGLS: DRAO H I INTERMEDIATE GALACTIC LATITUDE SURVEY

K. BLAGRAVE¹, P. G. MARTIN¹, G. JONCAS², R. KOTHES³, J. M. STIL⁴, M. A. MIVILLE-DESCHÊNES^{1,5},
FELIX J. LOCKMAN⁶, A.R. TAYLOR^{7,8,9}

Submitted to The Astrophysical Journal

ABSTRACT

Observations of Galactic H I gas for seven targeted regions at intermediate Galactic latitude are presented at 1' angular resolution using data from the DRAO Synthesis Telescope (ST) and the Green Bank Telescope (GBT). The DHIGLS data are the most extensive arcminute resolution measurements of the diffuse atomic interstellar medium beyond those in the Galactic plane. The acquisition, reduction, calibration, and mosaicking of the DRAO ST data and the cross calibration and incorporation of the short-spacing information from the GBT are described. The high quality of the resulting DHIGLS products enables a variety of new studies in directions of low Galactic column density. We analyze the angular power spectra of maps of the integrated H I emission (column density) from the data cubes for several distinct velocity ranges. Fitting power spectrum models based on a power law, but including the effects of the synthesized beam and noise at high spatial frequencies, we find exponents ranging from -2.5 to -3.0 . Power spectra of maps of the centroid velocity for these components give similar results. These exponents are interpreted as being representative of the 3D density and 3D velocity fields of the atomic gas, respectively. We find evidence for dramatic changes in the H I structures in channel maps over even small changes in velocity. This narrow line emission has counterparts in absorption spectra against bright background radio sources, quantifying that the gas is cold and dense and can be identified as the cold neutral medium phase. Fully reduced DHIGLS H I data cubes and other data products are available at www.cita.utoronto.ca/DHIGLS.

Subject headings: Radio lines: ISM – Methods: observational – Methods: data analysis – Instrumentation: detectors

1. INTRODUCTION

Atomic hydrogen is the most ubiquitous neutral component in the interstellar medium (ISM). Observations of its spin-flip transition at 21 cm have been used to map the distribution of H I on the sky, where it is found to exist not only in the Galactic plane but also at all Galactic latitudes and with a variety of velocities (e.g., Kalberla et al. 2005). Its distribution traces the neutral atomic ISM in both the warm phase (warm neutral medium, or WNM) and the colder denser phase (cold neutral medium, or CNM) and reflects the influence of the gravitational potential of the Milky Way galaxy and thermodynamic and dynamical effects. Although the spatial power spectrum of H I emission at intermediate and high Galactic latitudes is quite steep indicating that most structure in H I occurs on the largest scales (e.g., Miville-Deschênes et al. 2003a), there is important structure at these latitudes on angular scales $\lesssim 3'$ as evidenced in *Herschel* observations (e.g., Miville-Deschênes et al. 2010). These scales are

not sampled by existing single-dish 21 cm surveys: the southern hemisphere-based H I Galactic All-Sky Survey (GASS, Kalberla & Haud 2015); and in the north the Effelsberg-Bonn H I Survey (EBHIS, Winkel et al. 2016) and the deeper, targeted Green Bank Telescope (GBT) survey (GHIGLS, Martin et al. 2015).

To address this structure, arcminute resolution observations with an interferometer are required. Surveys in the Galactic plane include the Canadian Galactic Plane Survey (CGPS, Taylor et al. 2003), the Southern Galactic Plane Survey (SGPS, McClure-Griffiths et al. 2005), and the VLA Galactic Plane Survey (VGPS, Stil et al. 2006). H I has been studied at even higher resolution (20'') in the THOR survey (Beuther et al. 2016), which supplements the VGPS with data from the VLA C-array configuration. Surveys at higher latitude are less common but some have been carried out at the Dominion Radio Astrophysical Observatory (DRAO¹⁰) with the Synthesis Telescope (DRAO ST) (e.g., Martin et al. 1994; Miville-Deschênes et al. 2003a) and with the VLA closer to the plane (e.g., Pidopryhora et al. 2015). As described in this paper we built on the legacy of the CGPS by using the DRAO ST to map H I in seven regions at intermediate Galactic latitude during the period 2004 to 2012. This program is called DHIGLS (DRAO H I Intermediate Galactic Latitude Survey). The intermediate-latitude regions that we selected for the DRAO ST observations sample relatively faint H I emission, with both low and intermediate values of the neutral hydrogen column density (N_{HI}). They also sample a variety of gas components

¹ Canadian Institute for Theoretical Astrophysics, University of Toronto, 60 St. George Street, Toronto, ON M5S 3H8, Canada; blaggrave@cita.utoronto.ca

² Université Laval, Québec, PQ, Canada

³ Dominion Radio Astrophysical Observatory, Herzberg Institute of Astrophysics, National Research Council of Canada, Box 248, Penticton, BC, Canada V2A 6J9

⁴ Department of Physics and Astronomy, University of Calgary, 2500 University Drive NW, Calgary, AB, Canada T2N 1N4

⁵ Institut d'Astrophysique Spatiale, CNRS (UMR8617) Université Paris-Sud 11, Bâtiment 121, Orsay, France

⁶ National Radio Astronomy Observatory, Green Bank, WV 24944, USA

⁷ University of Calgary, Calgary, AB, Canada

⁸ University of Cape Town, Cape Town, South Africa

⁹ University of the Western Cape, Cape Town, South Africa

¹⁰ www.nrc-cnrc.gc.ca/eng/solutions/facilities/drao.html

distinguishable by their velocity (“velocity components,” hereafter VCs), spanning low, intermediate, and high velocity gas (LVC, IVC, and HVC, respectively).

The kinematic information in H I spectra provides essential diagnostics of various physical properties of the gas. The power spectrum of a map of H I emission can provide insight into the turbulent cascade in the ISM and the statistical description of the density and velocity fields. A direct correlation between the observed power law exponent and the energy and/or density structure, however, is not necessarily straightforward. From theory (Lazarian & Pogosyan 2000) and from fractional Brownian motion simulations (Miville-Deschênes et al. 2003b), the exponent of the power spectrum is expected to vary with the line-of-sight thickness of the medium, becoming steeper as this thickness exceeds the measured transverse spatial scales.

Miville-Deschênes et al. (2003a) provide an extensive discussion of empirical results. Observations of H I in the Galactic plane (Green 1993; Dickey et al. 2001; Green 2007) result in power spectra with power-law exponents ranging from -2.2 to -3.0 and values in the inner Galaxy span -3 to -4 . Hennebelle & Falgarone (2012) presented a graphical summary of spectral indices as a function of scale for various components of the ISM (see their Figure 10). Power laws associated with H I components appear to vary from shallow (-2.75) for H I in absorption (Deshpande et al. 2000) to steep (-3.6 ± 0.2) for LVC H I in emission in the Ursa Major Galactic cirrus studied by Miville-Deschênes et al. (2003a) using two pointings of the DRAO ST. The difference has been attributed to the H I lines in question tracing material at different temperatures: the colder ISM seen in H I absorption has a shallower power law than the relatively warm ISM that contributes to the H I emission.

High resolution H I spectra can also give insight to the properties of interstellar dust. Morphological spatial detail in maps of H I varies as a function of velocity, and so any dust closely correlated with a velocity component of the gas leaves a related morphological imprint in the dust emission map. This approach has been used to show that there is dust of significant emissivity associated with IVC gas (Martin et al. 1994). The selection of fields targeted by GHIGLS enabled exploration of the different kinematics and spatial distributions of H I gas and the dust evolution at diverse stages of Galactic evolution. GHIGLS data were used in combination with *Planck* data on thermal dust emission to find the emissivity, opacity, and temperature of dust associated with both LVC and IVC gas (Planck Collaboration XXIV 2011). At higher N_{HI} , excess dust emission above the correlation with H I suggests the presence of molecular hydrogen. With this motivation, Barriault et al. (2010) used DRAO ST spectra to investigate the atomic to molecular hydrogen transition in the diffuse ISM. Short-spacing information was supplied by the 26-m DRAO single dish. These DRAO ST syntheses are a subset of those used for the DF and UM regions (Table 1). However, the DHIGLS products presented here improve and expand on those data by increasing the size and depth of the mosaics and integrating short-spacing data from the 100-m GBT.

In the first part of the paper, which deals with the processing and quality assurance of the data, Section 2

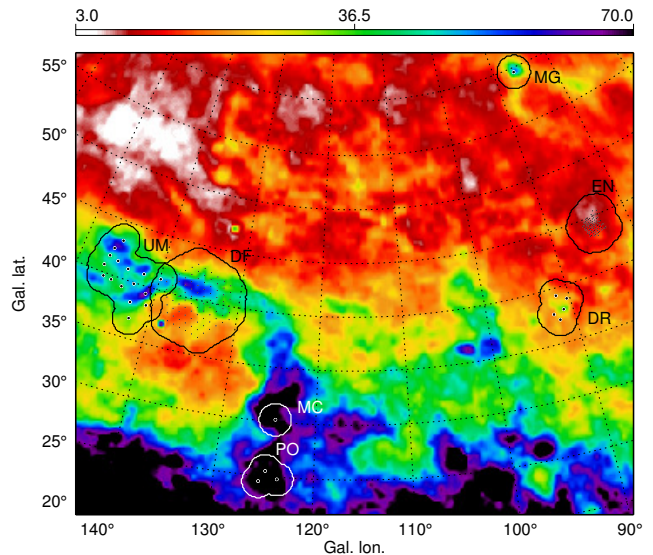


Figure 1. Locations of five DRAO ST mosaics and two single-pointing syntheses overlaid on a map of integrated H I emission from LAB in units of 10^{19} cm^{-2} . More details regarding the denser pointing centers are given in Section 3.2 and Appendix F.1.

describes the DHIGLS regions. In Section 3 the spectral line observations with the DRAO ST are introduced. Mosaicking of these data is described in Section 4. The process of combining the mosaicked DRAO ST interferometric data with single dish data from GHIGLS fields, which produces the DHIGLS products released with this paper, is discussed in Section 5.

The second part of the paper illustrates some of the science enabled by the data. Properties of the gas in distinct ranges of velocity (velocity components, or VCs) are introduced in Section 6, in particular maps of integrated H I emission (column density) and centroid velocities of the VCs. Several complementary power spectrum analyses of the H I gas are presented in Section 7. An exploration of some features of the observed CNM gas follows in Section 8. Section 9 summarizes the DHIGLS project and the main results of our first investigations with these new data. A description of the data available in the DHIGLS online archive is provided there.

There are several supporting Appendices. Appendix A details our implementation of analysis using the angular power spectrum. Complementary ranges of data in the u - v domain from interferometers and single dishes are assessed in Appendix B. Appendix C describes the cross calibration of the DRAO ST and GHIGLS data. The dependence of optical depth corrections on the angular resolution of the observations is explored in Appendix D. Appendix E revisits the results of some previous measurements of power spectra in the ISM. Supplementary details of the data and analysis for many DHIGLS regions are presented in Appendix F.

2. THE DHIGLS SURVEYS

Figure 1 shows the locations of the DHIGLS regions surveyed, overlaid on the map of H I emission integrated over velocity from the Leiden/Argentine/Bonn (LAB) survey (Kalberla et al. 2005). We note that by design all regions lie within GHIGLS fields as indicated in column 2 of Table 1. The GHIGLS H I data from the 100-m

Table 1
DHIGLS Regions Observed with the DRAO ST and GBT

DHIGLS Region	GHIGLS Field	Location ^a (α, δ)	Size ^a (deg ²)	DRAO ST Syntheses	v_c ^b (km s ⁻¹)	Δv ^b (km s ⁻¹)	Major ^c (arcsec)	Minor ^c (arcsec)
DF	SPIDER	10 ^h 30 ^m , 73 ^o 48′	57.4	DF00–DF90 ^d	−60	0.824	55.8 ± 0.7	53.7 ± 0.3
EN	N1	16 ^h 14 ^m , 54 ^o 49′	14.6	EN01–EN76	−60	0.824	65.7 ± 0.8	53.7 ± 0.4
MG	G86 ^e	14 ^h 41 ^m , 49 ^o 13′	7.1	MG	−20	0.412	71.8	53.4
DR	DRACO	16 ^h 48 ^m , 61 ^o 38′	12.5	MD PT–PW	−70 0	0.824 0.824	61.3 ± 0.5	53.7 ± 0.1
PO	POL ^e	02 ^h 57 ^m , 87 ^o 07′	10.7	LU LW ME	−25	0.412	53.9 ± 0.2	53.3 ± 0.2
MC	POL ^e	11 ^h 27 ^m , 86 ^o 42′	7.4	MC	−35	0.412	54.7	52.9
UM	UMA ^f	09 ^h 41 ^m , 68 ^o 33′	40.7	FP2 ^g NP MB ^h MH ^h NN ⁱ NW NX PK–PS	−60 −20 0	0.824 0.824 0.824	57.4 ± 0.7	53.6 ± 0.3

^a Central pixel of the final DHIGLS product and area within solid line contour in Figure 1.

^b Configuration of the 256-channel spectrometer: central channel velocity, v_c , relative to the Local Standard of Rest (LSR), and channel spacing, Δv .

^c Mean and dispersion of FWHM of synthesized beams for groups of syntheses that have been assembled into a mosaic.

^d Syntheses DF66/76/81/87 excluded (Figure 1 and Section 3.5).

^e Used GHIGLS raw data reprocessed to a “FINE” data cube with channel spacing 0.32 km s⁻¹ rather than 0.80 km s⁻¹ (Section 5.1).

^f GHIGLS NCPL combined field used for slightly larger spatial coverage (Section 5.1).

^g Same pointing as “Field 2” in Miville-Deschênes et al. (2003a).

^h Used the original MB and MH syntheses with channel spacing 0.412 km s⁻¹ and their repeats MB2 and MH2 with channel spacing 0.824 km s⁻¹ (Section 3).

ⁱ Same pointing as “Field 1” in Miville-Deschênes et al. (2003a), originally the EL field in Joncas et al. (1992) with early 4-antenna ST.

Robert C. Byrd Green Bank Telescope (GBT, Prestage et al. 2009) at the National Radio Astronomy Observatory (NRAO¹¹) over larger areas are used to fill in the low spatial frequency data missing in the interferometric observations (Section 5). In some later figures and in the DHIGLS data products these lower resolution single-dish data are also used to provide important spatial context for the DHIGLS observations outside the region studied with the DRAO ST.

DRAO ST data for our intermediate Galactic latitude mosaics were obtained between 2002 and 2012. The two deepest of these mosaics were originally conceived as a complement to anticipated *Planck* and *Herschel* observations. We refer to the one toward the GHIGLS field SPIDER as the “DRAO Deep Field” and denote both the region covered by mosaicked ST data and the final DHIGLS product as DF. The second of these is toward the GHIGLS field N1; we denote the mosaicked region and product as EN. Refer to Table 1 for a summary of the additional details of these and further DHIGLS mosaicked regions DR, PO, and UM and individual syntheses MG and MC.

2.1. Description of DHIGLS Regions and Science Goals

With the DRAO ST one cannot simply carry out an all-sky survey to map Galactic H I at arcminute resolution. Scarce resources (i.e., the number of syntheses) must be focused strategically. This section presents briefly why we selected certain fields to study. The details of the “resource allocation” to the DHIGLS regions and within

them (i.e., how the syntheses are placed), which relate closely to the science goals, are deferred to Section 3.2 and are summarized in column 5 of Table 1. Included in the science considerations is the availability of ancillary data (e.g., infrared imaging), which broadens the range of scientific investigations that are enabled by the DHIGLS data. To complement studies in the Galactic plane, the DHIGLS regions were selected to be at intermediate latitude and to have low to intermediate N_{HI} within a variety of VCs.

SPIDER¹² is a 10° GHIGLS field at the top of the arch of the North Celestial Pole Loop (NCPL), a giant gas structure north of the Galactic Plane with a cylindrical morphology (Meyerdierks et al. 1991). The related DHIGLS mosaicked region DF within this field focuses on the highly structured diffuse LVC emission. The IVC emission is much fainter and the HVC negligible. Targeted mapping of the stunning dust emission at even higher resolution has been carried out with *Herschel*.

The European Large-Area *ISO* Survey (ELAIS) N1 field is an “extragalactic window” targeted by the *Spitzer* SWIRE survey (Lonsdale et al. 2003) and most recently the HerMES legacy program on *Herschel* (Oliver et al. 2012). Its low column density can be appreciated in Figure 1. The GHIGLS field N1 spans 5°. ¹³ The DHIGLS mosaicked region EN focuses on the central lowest N_{HI} region. It has little LVC emission, negligible IVC emission, but striking HVC emission. At least at the GBT

¹² www.cita.utoronto.ca/GHIGLS/page1.php?v=GHIGLS_SPIDER_mini. See the movies on www.cita.utoronto.ca/GHIGLS/page1.php?v=GHIGLS_NCPL_mini for the larger-scale context of the structure in this field as a function of velocity.

¹³ www.cita.utoronto.ca/GHIGLS/page1.php?v=GHIGLS_N1_mini.

¹¹ The National Radio Astronomy Observatory is a facility of the National Science Foundation operated under cooperative agreement by Associated Universities, Inc.

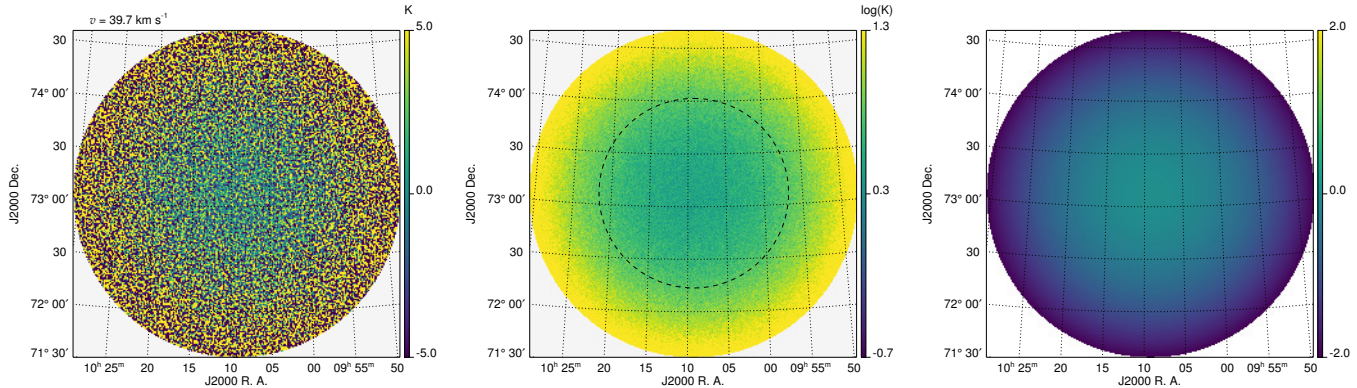


Figure 2. Left: single emission-free channel map from the representative single synthesis DF20, part of the DF mosaic. Correction for the primary beam amplifies the noise away from the center. Middle: noise map as determined empirically from the scatter over a number of emission-free channels of DF20, with logarithmic colorbar. Noise at center is 3.0 K. Dashed circle of radius $54'$ locates the FWHM of the primary beam of a 9 m antenna in the interferometer; there the noise is a factor of 2 larger than at the center because of the primary beam correction. At the outer boundary of radius $93'$ the noise has increased by a factor of 9.5 compared to the center, to 28.5 K. Right: corresponding model weight map, in logarithmic form, normalized to unity at the centre. Weight is $1/4$ at the FWHM circle and 0.011 at the outer truncation radius.

resolution the HVC gas morphology is not immediately obviously traced by dust and quantitatively the HVC has a low dust emissivity (Planck Collaboration XXIV 2011). The higher resolution DHIGLS observations enable a deeper search for HVC-correlated dust emission.

In addition to the Galactic ISM science, another goal for the two deepest DHIGLS regions (DF and EN) is to provide higher resolution H I data to complement the characterization of foregrounds at the $5'$ *Planck* resolution.

DRACO (Herbstmeier et al. 1993) was selected because of its prominent and distinctive IVC gas, which has a clear dust signature with *IRAS* and *Planck* (Planck Collaboration XXIV 2011). Targeted *Herschel* dust emission observations were carried out as well (Miville-Deschênes et al. 2016). The dynamics of the interaction of the IVC gas with the Galactic thick disk is fascinating and the transition from atomic to molecular gas in dense regions near the “interaction surface” can also be studied. Of course, the new observations here cover only the H I component. Differences in dust properties between LVC and IVC gas could provide evidence of dust evolution.

G86 is a prominent degree-sized high-latitude cloud found to have a clear signature of dust correlated with the IVC gas using early DRAO observations (Martin et al. 1994). A more sensitive single-pointing DRAO ST synthesis MG has been carried out, along with targeted *Herschel* imaging.

The DHIGLS region UM within the GHIGLS field UMA probes clouds with LVC gas spanning the transition from the diffuse H I phase to the molecular phase. A small two-pointing subregion of UM, which we refer to as URSA, has been studied previously using early DRAO ST data (Miville-Deschênes et al. 2003a; revisited in Appendix E) and imaged with *Herschel*.

The small DHIGLS region PO is the brightest part of the GHIGLS field POL and has molecular emission. Part of this region has been imaged with *Herschel* (Miville-Deschênes et al. 2010). We studied one other single-field synthesis, MC, within POL.

For a complete discussion of the DRAO ST and data reduction, refer to Landecker et al. (2000) and Taylor et al. (2003). Here we summarize some essential details for the H I data. The DRAO ST is an array of seven approximately 8.6 m antennas along an east-west baseline. A full synthesis contains data from baselines (antenna separations) in multiples of $L = 4.286$ m from $3L$ (12.86 m) to $144L$ (617.18 m) and takes 144 hours of observing time (12 h \times 12 antenna configurations). We note that while there are 21 baselines from 7 antennas, for H I data the S21 correlator forms only those baseline products needed for complete sampling of the Fourier plane, the 12 combinations involving a fixed and a movable antenna (Landecker et al. 2000); other combinations produce baselines that are redundant. For a field at Declination δ this sampling in the Fourier domain results in a synthesized beam of $49'' \times 49'' \csc(\delta)$ at 1420 MHz (Landecker et al. 2000).

For diffuse H I emission such as studied here, with structure on all scales, the presence of sidelobes in the dirty synthesized beam can both affect the fidelity of the image and reduce its sensitivity. To suppress the sidelobes a Gaussian taper is applied in the Fourier domain, attenuating the visibilities for the maximum baseline by 20%. Away from the main lobe the response of the synthesized beam falls below 0.5% everywhere in the field of view used (radius $93'$) and is typically more than an order of magnitude less (see Figure 2 in Taylor et al. 2003). This tapering results in a final beam of about $58'' \times 58'' \csc(\delta)$. To ensure proper sampling, maps from single syntheses are on grids with a pixel separation of $21''.875$ while final DHIGLS mosaicked products are on grids with a pixel separation of $18''$.

In this paper, velocities are relative to the Local Standard of Rest (v_{LSR}). The spectrometer has 256-channels and the coverage was centered on $v_{\text{LSR}} = v_c$ with v_c varying for each mosaic as in Table 1. Channels were spaced every 0.824 km s^{-1} and the velocity resolution was 1.32 km s^{-1} . As noted in Table 1, a few syntheses were observed with a finer channel spacing of 0.41 km s^{-1} (or a central channel velocity of 0 km s^{-1}) leading to reduced spectral coverage (toward negative velocities).

3.1. Noise and Weight Map for a Single Synthesis

Understanding the noise properties of any telescope is necessary to inform an observing strategy. Three maps related to the noise in a single synthesis are illustrated in Figure 2. The differences in each of these representations are discussed below.

Inspection of an emission-free channel map from this single DHIGLS synthesis indicates that the typical rms noise for 0.824 km s^{-1} channels is 18 mJy beam^{-1} (or $3.2 \sin \delta \text{ K}$). In fact, noise estimates for all syntheses compare well to the value measured for the original phase of the CGPS carried out in the previous decade (Taylor et al. 2003), $3.2 \sin \delta \text{ K}$.

For astrophysical applications of a single synthesis, we need to correct each channel map by the primary beam of a 9 m antenna (the effect of its attenuation), which amplifies the noise away from the center. We note that the primary beam is not a Gaussian, but is well described by a \cos^6 function of radial offset (Taylor et al. 2003) with a FWHM of $108'$. The corrected emission-free channel maps are therefore noticeably noisier around the periphery, as shown in the left panel of Figure 2.

The noise can also be quantified by finding the rms in the spectrum over many emission-free channels pixel by pixel; after correction for the primary beam this gives us an empirical “noise map” as in the middle panel. In making a mosaic, the contribution from a single synthesis is weighted according to the inverse square of the noise. The model for the weight map is therefore the square of the primary beam, here normalized to unity at the pointing center (there is no dependence of the central value on δ as in the noise map). This map is shown in the right panel.

Each of the maps is truncated at a radius of $93'$, where the noise has risen by a factor 9.5 compared to the value at the pointing center and the weight has fallen to 0.011 (see Figure 2). As adopted for the CGPS, data beyond this radius are not used in assembling the mosaics (Section 4.1).

3.2. Planning Mosaics

In a single synthesis the rms noise level for a single channel varies across the field (Figure 2). The noise level can be made more uniform and/or greatly reduced by assembling a number of single syntheses as a mosaic. For example, the CGPS mosaic pattern was that of a close-packed hexagonal grid with pointing centres separated by $112'$, a bit larger than the FWHM, a compromise between uniform sensitivity and spatial coverage at 1420 MHz. With this in mind, for the much fainter EN region we chose a pattern of single pointings to emphasize sensitivity over spatial coverage with spacings of about $12'$, while for the brighter DF we opted for more extended coverage with spacings of about $40'$. Figures 3 and 4 show the pointing centers for DF and EN, numbering 91 and 76 respectively (see Table 1). These figures are in ICRS coordinates (α, δ) and the NCP projection (Calabretta & Greisen 2002) native to the DRAO ST data. The central position of each synthesis field is marked by a bullet. For scale, we show the FWHM of the primary as a dashed circle of diameter $108'$. Also shown as the solid circle is the $93'$ truncation radius ($186'$ diameter) used in the production of the final mosaic.

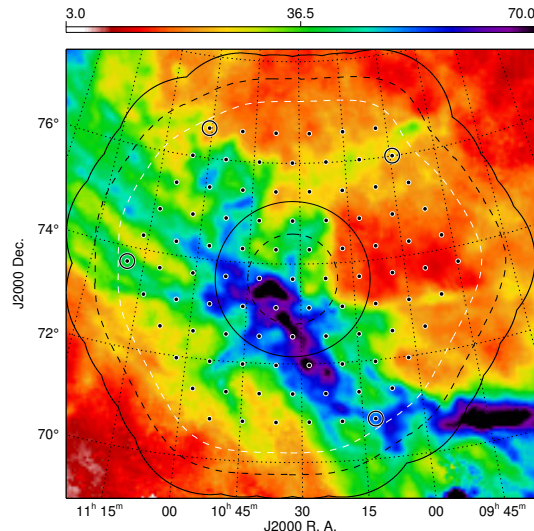


Figure 3. Synthesis pointing centers chosen for the mosaic of the DF region, each of the 91 marked by a bullet; 4 marked with a circle not included because of calibration uncertainty. Background is integrated emission from GHIGLS NCPL combined field in units of 10^{19} cm^{-2} . For the highlighted pointing DF00 ($10^{\text{h}}32^{\text{m}}17^{\text{s}}, 73^{\circ}42'0''$) primary beam FWHM and mosaic truncation radius (Section 4.1) are shown with dashed- and solid-line circles, respectively (corresponding circles seen in single synthesis field DF20 in Figure 2). Dashed- and solid-line contours near edge of mosaic trace constant noise levels as discussed in Section 4.2.

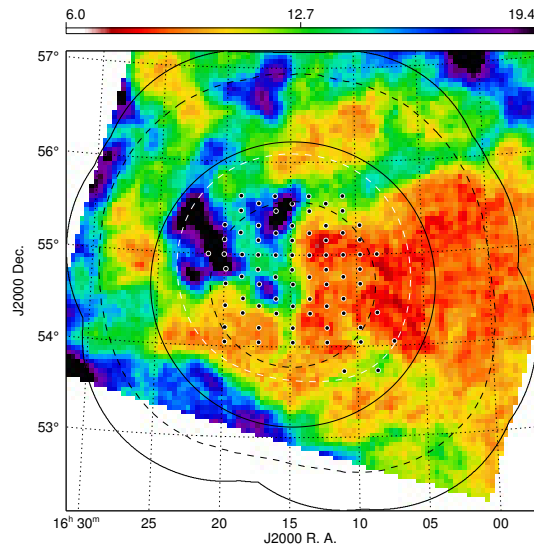


Figure 4. Same as Figure 3, but for the 76 pointings making up the mosaic of the EN region, with highlighted pointing EN18 ($16^{\text{h}}14^{\text{m}}48^{\text{s}}, 54^{\circ}40'57''$). Note the difference in angular scale and the colorbar between these two figures.

The pointing centers for the other mosaics of DHIGLS regions are given in Figure 1 and Figure F.1.

3.3. Characterizing the Beam

A synthesized beam for each of the fields was produced corresponding to the visibility coverage in the Fourier domain. This beam was normalized to unity at its center. Because much of the data processing involves approximating the beam with a Gaussian, the synthesized beam was fitted in the image domain with a two-dimensional

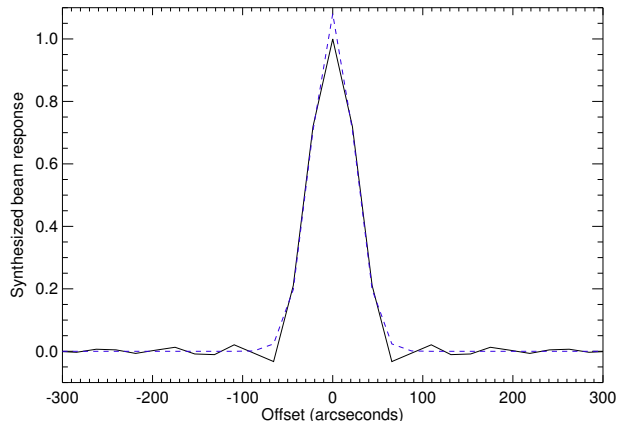


Figure 5. Cross section in Declination of the synthesized beam. Overlaid red line indicates that the Gaussian model overpredicts the peak brightness of a point source.

(2D) Gaussian to determine the effective beam size. The effective beam size was consistently smaller than the half-power beam-width (HPBW) of $58''$ and consistently peaked at 1.08 with a relative beam integral of 1.08 (see Figure 5). The mean Gaussian FWHM of the synthesized beam and its dispersion for the mosaic is given in Table 1 for each region.

3.4. Continuum Removal

Two continuum maps are produced from an average of the channels at each end of the spectrum that are free of H I emission. The channel selection is performed independently for each synthesis with the median number of channels used for a continuum map being 30, separately for each end. The continuum contribution at each channel in the spectral cube is then determined by linear interpolation between these two continuum maps. Empirically there is only a minimal frequency dependence of the continuum over the frequency range of the data cube and so in the few exceptional cases where there are emission-free channels at only one end of the spectrum the resulting single continuum map is subtracted directly from the spectral cube.

In a number of fields there are very bright point sources that produce correspondingly bright artifacts in the form of grating rings. Subtraction of the continuum will in principle remove the continuum source and any artifacts around it. However, within the spectral cube the continuum emission could be absorbed by diffuse H I in some channels, resulting in a weaker point source and a concomitantly weaker set of artifacts in those channels. Following subtraction of the unattenuated continuum, a scaled negative imprint of the source and artifacts would remain in those absorbing channels. For weaker point sources, the artifacts are hidden in the noise but to mitigate such potential residual contamination for bright sources it is useful to create a clean cube prior to producing the continuum maps, by deconvolving those bright point sources with a model beam. This cleaning process follows routines developed for the DRAO ST by Willis (1999) and is performed on each channel in a given cube. It is performed only on those cubes having continuum point sources with flux density $F > 1 \text{ Jy beam}^{-1}$ and this cleaning proceeds down to the level of $300 \text{ mJy beam}^{-1}$

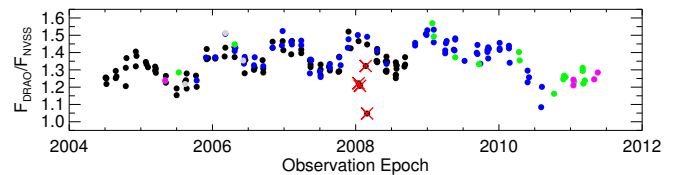


Figure 6. Temporal variability of the $F_{\text{DRAO}}/F_{\text{NVSS}}$ scale factor (typical uncertainty 0.03). Syntheses for regions DF (black), EN (blue), UM (green), DR (magenta), and other pointings (grey) show a consistent trend. Four syntheses in DF that have strong asymmetric ring artifacts in the point-source continuum maps also show the strongest deviations from the trend (marked with a red cross), supporting the view that the scale factors for these are unreliable. Off the plot is a lone field FP2 at epoch 2012.8 with scale factor 1.53.

as was done in the CGPS (Taylor et al. 2003).

3.5. Position Registration and Flux Density Scale

An averaged continuum map was produced for each synthesis from the two continuum maps. Each point source in this map was fitted with a 2D Gaussian (with the `fluxfit` routine included in the DRAO Export Software Package `madr`, Higgs et al. 1997) to determine its sky coordinates (α, δ) and flux density F_{DRAO} , limiting the width of each fit to be no less than 95% of the effective beam parameters determined in Section 3.3.

The fitted values were compared with those in the NVSS¹⁴ database (Condon et al. 1998) to determine for each field a weighted average offset in sky coordinates ($\Delta\alpha, \Delta\delta$) and a weighted average flux density ratio, $F_{\text{DRAO}}/F_{\text{NVSS}}$. Taylor et al. (2003) discuss this in detail. We find values of the flux density ratio $F_{\text{DRAO}}/F_{\text{NVSS}}$ in the range 1.2 to 1.5; the typical uncertainty for each determination is 0.03.

Because the synthesized beam is not quite Gaussian, F_{DRAO} measured by Gaussian fitting will be overestimated by a factor of about 1.08 (Section 3.3). We note that in the conversion from surface brightness to brightness temperature (see Section 4) this factor of 1.08 returns in the amplitude of the Gaussian-fitted beam and so it cancels out.

A plot of $F_{\text{DRAO}}/F_{\text{NVSS}}$ for all DRAO ST syntheses as a function of observation date reveals intriguing systematic variations (Figure 6). This is present in the data used in a single mosaic (e.g., regions DF and EN colored separately) and for the interleaved observations, ruling out a dependence on Declination. There might be a seasonal trend, though it is not exactly the same year to year. We note that changes in the equivalent VLA to NVSS ratio cited as part of the VGPS (Stil et al. 2006), though also not fully understood, were shown to be related to the band-averaged scalar amplitude of the continuum-subtracted visibilities, which is in turn connected to the noise.

The empirical pattern of the temporal variation is useful for confirming suspected anomalous $F_{\text{DRAO}}/F_{\text{NVSS}}$ scale factors. A few fields have strongly asymmetric ring artifacts in the point-source continuum images and were suspected of having inaccurate ratios, and we found that these fields (DF66, DF76, DF81, and DF87), observed in late 2007/early 2008, have the largest deviations from

¹⁴ www.cv.nrao.edu/nvss/.

the trend seen in Figure 6 (each marked with a red cross). Therefore, these fields at the edge of the DF region were excluded.

4. MOSAICS MADE USING INTERFEROMETRIC DATA FROM THE DRAO ST

In this section we focus on mosaics assembled from the DRAO ST data at many adjacent pointing centers. To distinguish this intermediate product that uses only data from the interferometer from the final DHIGLS product that also incorporates short-spacing information from the GBT data (Section 5) we append “-i” to the name of the region mosaicked, for example DF-i.

4.1. Assembling the Mosaic

As described in Section 3.2, our DRAO ST observations were designed with the intent of combining several syntheses with adjacent pointing centers into a mosaic. For each synthesis the DRAO ST data cube (in Jy beam^{-1}) was converted to brightness temperature, T_b , using the beam parameters determined in Section 3.3 and the scale factor determined from the comparison with NVSS (Section 3.5). The channels of each synthesized cube were then interpolated to a common velocity grid using a spline interpolation. This interpolation has very little effect on the spectra, but is required to ensure a consistent velocity grid among all fields.

The prepared data from the individual syntheses were then assembled into mosaics using the routine SUPERTILE in `madr`. As described by Dewdney et al. (2002) and Taylor et al. (2003), SUPERTILE reads in the position registration results for each of the fields (Section 3.5), adjusts the position of each field accordingly, divides by the DRAO ST primary beam (which amplifies the noise away from the beam center), truncates each data set at a radius of $93'$ relative to its pointing center, and combines the data, keeping track of the beam shape and weights throughout the process.

4.2. Noise and Weight Maps for Mosaics

The channel maps of the mosaicked H I spectral line data are contained in a data cube. We can produce a noise map from emission-free channels as we did for a single synthesis in Section 3.1. An example is shown in the upper panel of Figure 7 for the DRAO ST DF-i mosaic. The corresponding weight map produced in assembling the mosaic is shown in the lower panel.

Figure 7 shows the distinctive pattern of increased noise around the perimeter as a result of the lower coverage and effect of the primary beam there. Across most of the field the noise is 1.0 K, clearly reduced compared to 3.0 K for a single synthesis because of the chosen dense packing of pointing centers (and the typical non-unity scale factor $F_{\text{DRAO}}/F_{\text{NVSS}}$ applied to the single syntheses prior to mosaicking).

We note that because of the weighting scheme used in SUPERTILE, the weight map can be used to create a theoretical noise map by multiplying its inverse square root by the typical noise for a single synthesis, $3.2 \sin \delta$ K (modified by the typical $F_{\text{DRAO}}/F_{\text{NVSS}}$ scale factor for the syntheses in the mosaic). Therefore, in figures for other regions below we display only the noise map.

The noise map is used to create three contours. Two contours, e.g., black outer dashed and solid contours in

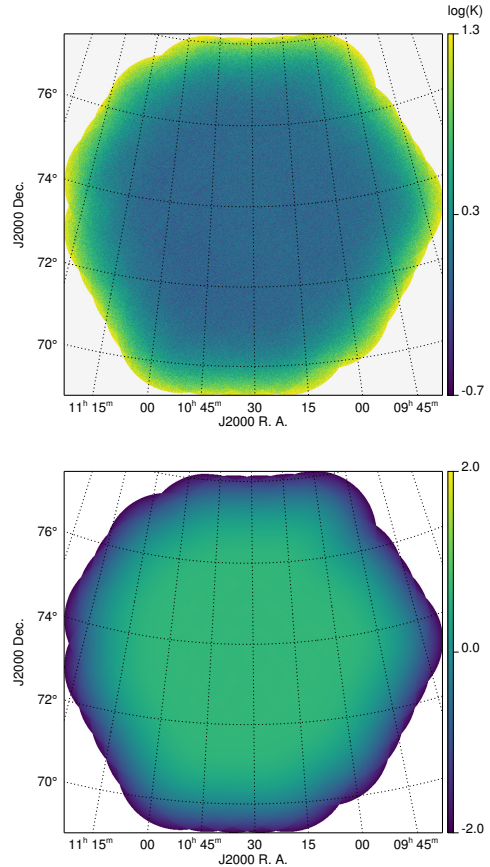


Figure 7. Maps displaying the noise (upper panel) and the relative weight (lower panel) across the DF-i mosaic. Adopting the same logarithmic colorbar scales as in Figure 2 emphasizes the improvement compared to the corresponding values for the single synthesis DF20.

Figure 3, indicate where the noise of the mosaic is identical to the noise in a single synthesis at the FWHM of the primary beam and at the truncation radius, respectively. A third contour, e.g., white dashed in Figure 3, indicates where the noise is only a factor of two larger than in the central, lowest-noise region, thus selecting a low-noise portion of the larger mosaic (inside the outer black dashed contour because the central noise in the mosaic is lower than for a single synthesis). The white dashed contour is of particular significance in selecting data for analyses discussed below.

We have carried out a similar analysis for the EN-i mosaic. The noise map is shown in Figure 8. This clearly shows that the denser packing of pointing centers of the syntheses making up the mosaic (Figure 4) has significantly reduced the noise in the central region to 0.3 K, about a factor of 3 lower than in DF-i. The denser packing also reduces the relative extent of the low-noise region marked by the dashed white contour in Figure 4.

Likewise, noise maps for the UM-i mosaic and the smaller DR-i and PO-i mosaics are presented in Figures F.2, F.5, and F.8 in Appendix F.

4.3. H I Signal Maps

Figure 9 shows a representative channel map of the H I signal in the DRAO ST DF-i mosaic near the peak of the average spectrum. Below we analyze the power spectrum in a low noise (and high signal to noise) region shown in

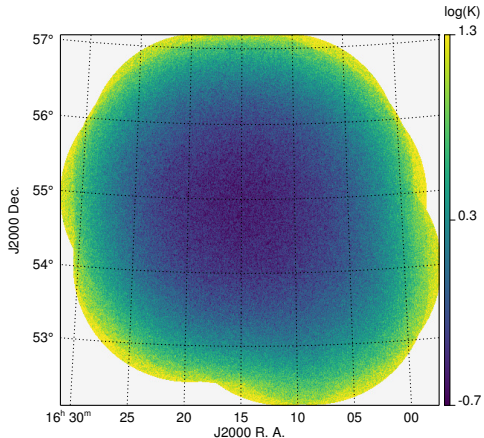


Figure 8. Noise map as in upper Figure 7, for EN-i mosaic.

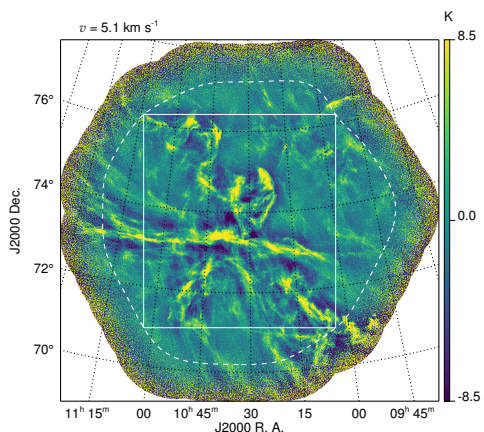


Figure 9. Channel map from DF-i mosaic ($v = 5.1 \text{ km s}^{-1}$, in the LVC range). Region used in calculation of power spectrum in Figure 11 is indicated by a white rectangle (see Section 4.3).

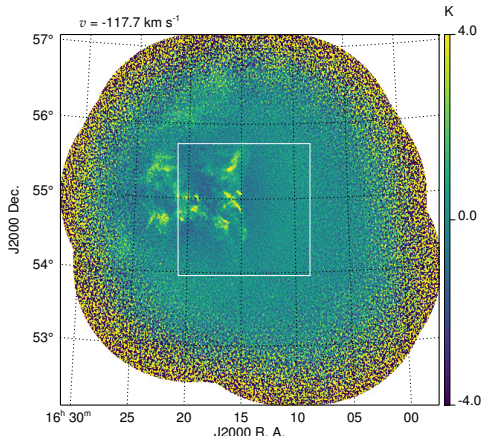


Figure 10. As in Figure 9, for EN-i mosaic and $v = -117.7 \text{ km s}^{-1}$ in the HVC range. White rectangle indicates region used for power spectrum analysis in Figure 12.

Figure 9 as the “white rectangle.” This is the rectangle of largest area that is aligned with the pixel grid and fits inside the “white dashed contour” defined in Figure 3, which is the region of least noise.

Similar data are shown in Figure 10 for the EN-i mosaic and in Figures F.2, F.5, and F.8 for the UM-i, DR-i, and

PO-i mosaics in Appendix F.

4.4. Insight from the Angular Power Spectrum

It is of interest to relate the signal and noise in H I maps to their manifestations in the Fourier domain (harmonic or u - v domain) and the angular power spectrum. In addition to enabling the science application discussed in Section 7, this provides a means of exploring the sensitivity of synthesis telescope observations to various spatial scales and more immediately allows for direct comparisons with (and integration of) observations from single-dish telescopes, as will be described in Section 5. Facilitating such analyses is the power spectrum model development including the “noise template” and fitting presented in Appendix A building on earlier work described in Miville-Deschênes et al. (2007) and Martin et al. (2015).

The 2D angular power spectrum of a map $f(x, y)$ (image of the sky) is the square of the modulus of the Fourier transform $\tilde{f}(k_x, k_y)$ (the visibility) where k is the spatial frequency (wavenumber) in the u - v domain:

$$P(k_x, k_y) = |\tilde{f}(k_x, k_y)|^2. \quad (1)$$

The collapsed one-dimensional (1D) power spectrum $P(k)$ is formed by azimuthal averaging of $P(k_x, k_y)$ in annuli of constant $k = (k_x^2 + k_y^2)^{1/2}$. We use this for both analysis and display purposes (see Appendix A.5 for exceptional images with directional structure).

The 2D Fourier transform reflects the sampling in the u - v domain, which is quite uniform for the DRAO ST syntheses, with noise increasing at angular frequencies with little or no coverage. Depending on the symmetry of the Fourier transform, differing amounts of this structure will remain in $P(k)$. In the limit where the synthesized beam is circularly symmetric, there is a direct mapping of the features in the 2D power spectrum to the 1D $P(k)$. Of the two deepest mosaics, DF-i is much closer to this limit than is EN-i.

Figure 11 shows $P(k)$ for the LVC H I channel map in Figure 9 for DF-i. There the data have been fit to the 1D power spectrum formed after deconvolution in 2D using the asymmetrical synthesized beam. The fit to the power law model of Equation (A1) has power law exponent $\gamma = -2.99 \pm 0.04$ and scales the noise template by $\eta = 1.59 \pm 0.03$. We also show an alternative representation in which the modelling is carried out without deconvolution, requiring accounting for the lowering of power by the effective beam at high spatial frequencies (see Equation (A2)). These parameters are consistent with those found above: $\gamma = -3.03 \pm 0.03$ and $\eta = 1.60 \pm 0.03$.

To assess the level of noise achieved and the ability to investigate the variety of spatial structure using the DRAO ST H I data, we have modelled the power spectra in the other regions mosaicked, in Figure 12 for the single channel maps shown in Figures 10, F.2, F.5, and F.8.

As in DF-i, the denser coverage in EN-i also lowers the power spectrum of the noise, so that as seen in Figure 12 the power spectrum of the signal can still be analyzed over a considerable range in k , even though the H I signal in this channel is much weaker than in the channel selected for DF-i. Here the noise template is scaled by $\eta = 1.22 \pm 0.09$. Generally η decreases toward 1.0 as the H I signal diminishes, and vice versa. The

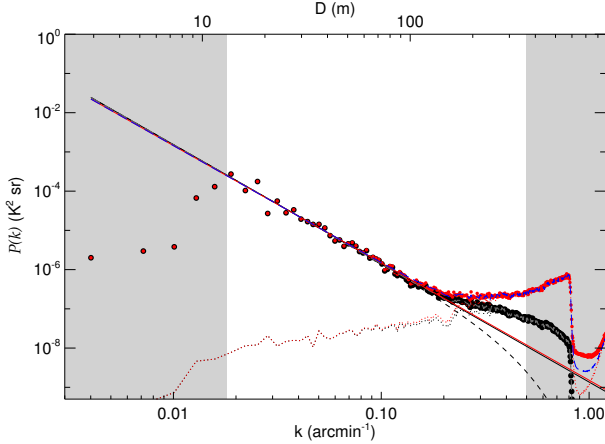


Figure 11. Power spectra of the DF-i mosaic for signal channel in the LVC range and white rectangle region shown in Figure 9. Data in red result from deconvolution by the 2D synthesized beam. Data in black are without deconvolution. Dotted curves are the scaled noise component, solid lines are the power-law component and long dashed curves are the total power spectrum model (Equations (A1) and (A2)). Black dashed curve shows the modification of the power-law by the synthesized beam. Data in shaded ranges of k were excluded from the model fit (see Appendix A.3).

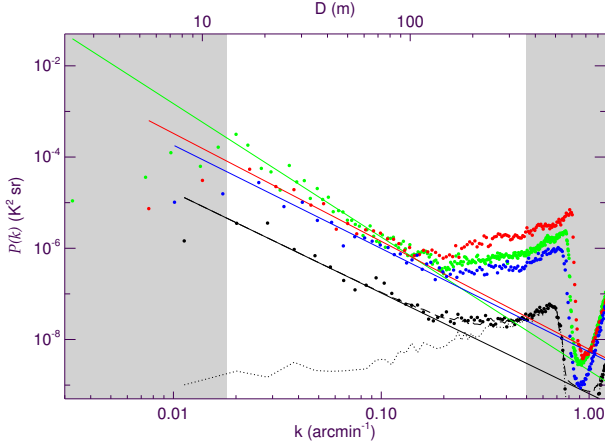


Figure 12. Power spectra from the EN-i mosaic (black, HVC), UM-i (green, LVC), DR-i (blue, IVC), and PO-i (red, IVC) for channel maps and white rectangle regions shown in Figures 10, F.2, F.5, and F.8, respectively, at same scale as for DF-i in Figure 11. For EN-i the noise (dotted line) is lower than in DF-i and so despite the signal being even lower the power spectrum of the signal can still be analysed over a significant range of k . For the others, both signal and noise are higher than in DF-i.

power law for this HVC channel is significantly shallower ($\gamma = -2.21 \pm 0.12$) than that for the LVC channel in DF-i ($\gamma = -2.99 \pm 0.04$).

For the remaining UM-i, DR-i, and PO-i power spectra in Figure 12, at high k where the noise dominates, the different levels are in accord with expectation based on the noise maps presented in Section 4.2 and Appendix F. Similarly, the values of η show the expected differences with H I signal strength, being 1.40 ± 0.03 , 1.04 ± 0.05 , and 1.27 ± 0.05 for the selected channels in UM-i, DR-i, and PO-i, respectively. Despite the different noise levels and signal strengths, the power spectrum of the signal can still be analysed over a significant range of k .

Extending the comparison made between DF-i and EN-i, the power spectrum falloff for the UM-i LVC chan-

nel is similar to that for DF-i, but visibly steeper than for the HVC channel in EN-i; this is quantified in the power-law exponent, -2.93 ± 0.08 . On the other hand the data for the IVC channels in DR-i and PO-i appear more compatible with the behaviour in EN-i. Their exponents are -2.27 ± 0.14 and -2.4 ± 0.2 , respectively.

Thus the data are of sufficiently high quality that some differences can be discerned. However, because these power spectra are for individual channels and are thus responding to a mixture of velocity and density fluctuations (Lazarian & Pogosyan 2000) the exponents cannot be linked simply to the structure of the atomic gas. This will be followed up in Section 7.

5. INCORPORATION OF DATA AT LOW SPATIAL FREQUENCY

A synthesis telescope with moveable antennas provides ample coverage at discrete frequencies in the angular frequency domain, but is not sensitive to angular frequencies below that corresponding to the closest antenna spacing (some foreshortening of the baselines during a synthesis observation provides some sampling of lower spatial frequencies, but not much sensitivity). In the case of a DRAO ST synthesis, this is 13 m (Section 3) or $0.018 \text{ arcmin}^{-1}$ (Figure 11 and Appendix A.3).

To fill in this short-spacing information, observations using a filled aperture are required. Many of the issues related to how this is accomplished are discussed in Stanimirovic (2002).

Historically, for the DRAO ST, data from the DRAO 26 m telescope have been used most often (e.g., Higgs & Tapping 2000; Taylor et al. 2003; Higgs et al. 2005). However, as discussed in Appendix B, that telescope is not ideally sized to maintain sensitivity through the transition region in angular frequency where the coverage of the single filled aperture and the interferometer overlap.

By contrast, in DHIGLS we combined the DRAO ST data with complementary data from the GBT, whose 100 m diameter is 7.8 times larger than the shortest baseline in the DRAO ST. As illustrated in Figure B.1 in Appendix B and discussed below, using GBT data greatly improves both the width of and the sensitivity in the transition region and allows more choice in optimizing the addition of the short-spacing data.

5.1. GHIGLS Observations and Cross Calibration

We adopted observations made with the GBT as part of GHIGLS (Martin et al. 2015). On-the-fly observations of the fields produced Nyquist-sampled maps with an effective GHIGLS beam slightly elongated in the scanning direction. The GHIGLS beam can be modelled accurately in 2D and when approximated by a 2D Gaussian is $9'55 \times 9'24$ FWHM (Martin et al. 2015). The data reduction pipeline for calibration of these H I measurements, the correction for stray radiation, and baseline removal is described in Boothroyd et al. (2011) and Martin et al. (2015). The spectrometer channel spacing in the final GHIGLS data cubes is 0.80 km s^{-1} with velocity coverage well over $\pm 200 \text{ km s}^{-1}$, i.e., beyond that covered by the DRAO ST. For use with the higher velocity resolution data in the PO-i mosaic and the MC and MG single syntheses from the DRAO ST (Table 1), we reprocessed the archived GBT raw data to create POLFINE and G86FINE data cubes with channel spacing 0.32 km s^{-1} .

The large SPIDER field was observed in $2^\circ \times 2^\circ$ segments and then assembled into a final $10^\circ \times 10^\circ$ cube. The nine central sections of SPIDER were measured twice. Other relevant GHIGLS fields (Table 1) are N1 (measured 2 times), G86 (3), DRACO (3), POL(1), and UMA (1). The typical end-channel (emission-free) rms noise is 105 mK per observation, reducing to 75 mK for two observations (appropriate to the central region of SPIDER). For the reprocessed G86FINE and POLFINE fields, the noise is typically 96 mK and 170 mK, respectively. Note that for the DRAO ST UM-i mosaic we actually used the GHIGLS NCPL combined field to achieve slightly greater spatial coverage.

Each synthesis pointing used in the assembly of a given DRAO ST mosaic has been registered and scaled to the NVSS flux scale as described in Section 3.5. However, here we are interested in having a consistent calibration between the H I data from the DRAO ST mosaic and GHIGLS. To this end, as described in Appendix C, we determined a cross calibration scale factor for the brightnesses, $f_{cc} \equiv I_{\text{GBT}}/I_{\text{DRAO}} = 1.12 \pm 0.01 \pm 0.03$, that is to be applied to the DRAO ST mosaicked H I data to bring them to the GHIGLS scale.

5.2. Combining Data from GHIGLS Fields and DRAO ST Mosaics

As described below, we combined the two data sets by weighting their Fourier transforms. We refer to the DRAO ST + GHIGLS product as the “combined” (or “merged”) image. This combined product is the one contained in the DHIGLS data cube and the spectra therein are on the GHIGLS scale.

Our approach to weighting is close to that of the AIPS task IMERG.¹⁵ Using the *madr* software, the transformed data below some k_{min} are taken from the GHIGLS data and above some k_{max} from the DRAO ST data, and within this “image combination overlap range” the data are weighted by complementary functions summing to unity. We used a cubic polynomial in k with zero slope at the inner and outer edges of the range. Note that the overlap ranges for the cross calibration and the image combination need not be the same. However, because many of the same considerations apply (see Appendix C.2) we did adopt the same range. We note again that this k_{max} is well below the range affected by the DRAO ST synthesized beam. Refer to Figure B.1 in Appendix B.

This approach is different than the CASA task *feather*¹⁶ and IMMERGE (Stanimirovic 1999; Sault & Killeen 2011) in two ways. First, these use $k_{\text{min}} = 0 \text{ arcmin}^{-1}$ and so despite the weighting function applied, the interferometric data are used below the range actually sampled in the $u-v$ domain. Second, the weighting function applied to the deconvolved single-dish data is simply the Fourier transform of the single-dish beam and so with no restriction on k_{max} other than implied by the decreasing weight, data strongly affected by the noise are incorporated. Our adopted limits to the range address both of these issues.

In the combined image we are interested in preserving the high resolution information in the DRAO ST mosaic

¹⁵ <http://www.aips.nrao.edu/cgi-bin/ZXHLP2.PL?IMERG>

¹⁶ <http://casa.nrao.edu/docs/TaskRef/feather-task.html>

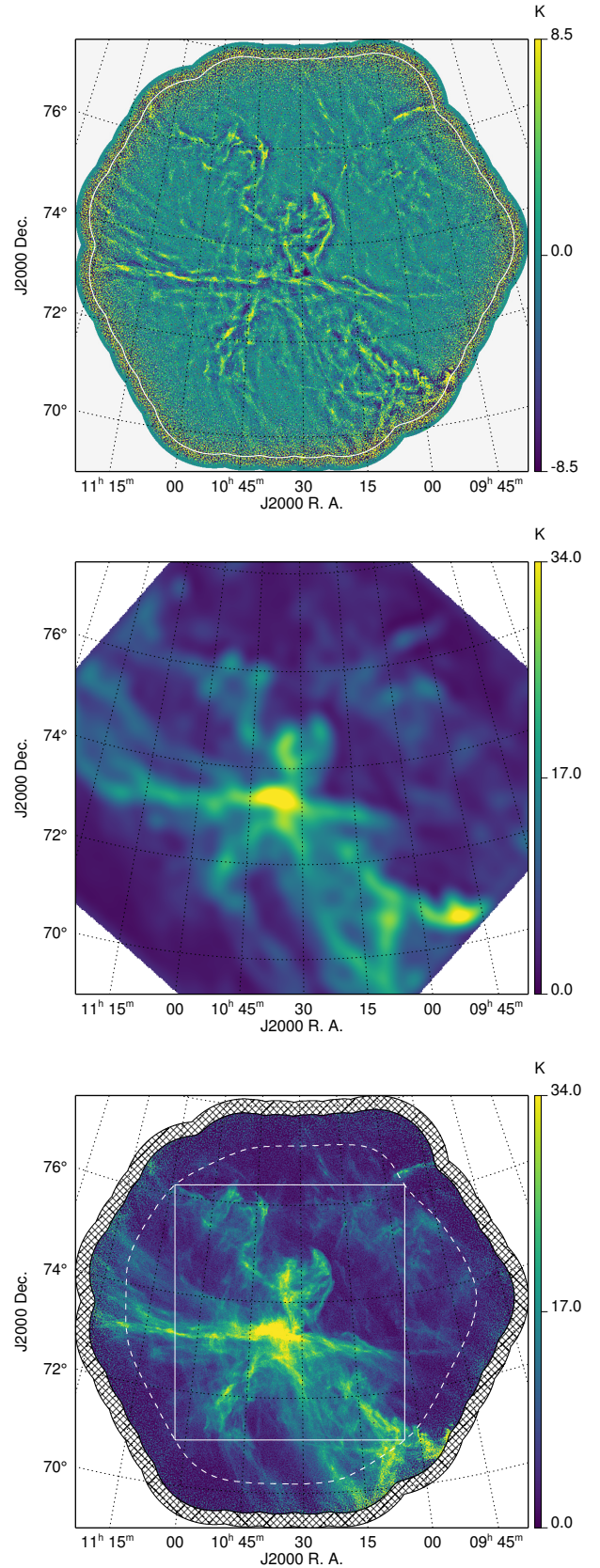


Figure 13. Channel maps for DF at $v = 5.1 \text{ km s}^{-1}$ as in Figure 9. Upper and middle: high and low resolution filtered images, respectively. Lower: Their addition, the final DHIGLS product. See Section 5.2 for details of the annotations and Section 5.3 for discussion.

and so we use that mosaic, scaled by f_{cc} , in its original ICRS coordinate system. To reduce edge effects from the conversion to the Fourier domain, the image is apodized with a taper beginning $10^{\circ}9$ from the edge and ending at the outer contour of the mosaic. For details on the apodization of non-rectangular fields, refer to Appendix A.4. The apodized and zero-padded image was Fourier transformed, the weighting function applied in 2D, and then the data were back transformed, producing a “high resolution” filtered image. An example for a single channel of DF-i is shown in the upper panel of Figure 13. Pixels exterior to the inner edge of the apodized region (see contour in this panel) were flagged for exclusion in the combined cube.

The original GHIGLS data were interpolated to the velocity channels of the DRAO ST data and initially to a 1.5 ICRS grid centered on that of the DRAO ST mosaic. It is sufficient to have a rectangular region somewhat larger than the mosaic. This image was median-subtracted, apodized, Fourier transformed, and then deconvolved with a 2D Gaussian approximation of the GHIGLS beam. Subsequently, the weighting function was applied and the data back transformed to produce a second “low resolution” filtered image, which was finally regridded to the finer grid of the DRAO ST mosaic. An example corresponding to the same channel is shown in the middle panel of Figure 13. As done for the DRAO ST data, pixels affected by the apodization of the GHIGLS data are flagged for exclusion.

The high and low resolution filtered data were combined (added) in the image plane. To complete the example for the single channel in the DF region, this final product is presented in the lower panel of Figure 13. Pixels in hatched area (affected by the apodization of the low resolution filtered image) and beyond are encoded as zero in a modification of the weight map provided as an extension to the DHIGLS cube (Section 9).

This procedure was carried out for each velocity channel to produce the DHIGLS cube. The final data products are cropped in the x- and y-directions to exclude the hatched region and the remaining blank and hatched region pixels are filled with the regridded original GHIGLS data for context. Before any analysis these can be removed (masked) using the modified weight map supplied with the data cube. DHIGLS data cubes are available on a public archive, as described at the end of Section 9. For any processing of these data cubes (e.g., convolving to the native resolution of another instrument such as *Planck*), take note of the synthesized beam parameters in Table 1.

5.3. Assessment of the Short-spacing Correction

H I emission has structure on all scales for which a power spectrum in the $u-v$ domain provides a useful statistical quantification. The power spectrum of the combined channel map in Figure 13, for the data within the white dashed contour, is given in Figure 14. Given how the combined map was constructed, the power spectrum for values of k higher than the overlap range (in blue) is identical to the power spectrum of the scaled interferometric data alone (shown in red, but for clarity only for $k < 0.05 \text{ arcmin}^{-1}$). Because of the broad overlap in $u-v$ coverage the latter power spectrum actually agrees quite well through most of the overlap region, before even-

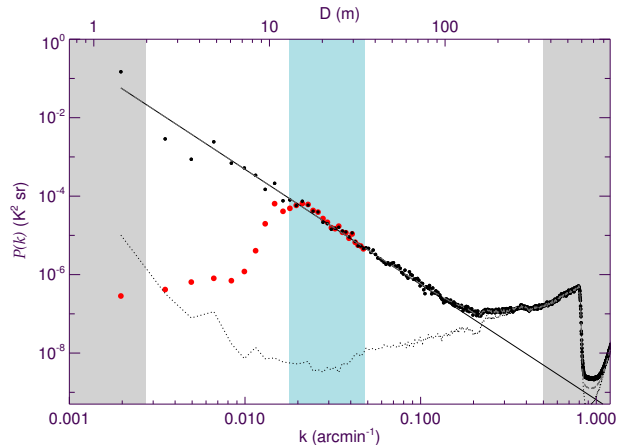


Figure 14. Power spectrum of single channel at $v = 5.1 \text{ km s}^{-1}$ as in Figure 11, but for the combined DRAO ST + GHIGLS DF image and for data within the white dashed contour (Figure 13). Model fit is to deconvolved data using Equation (A1). The blue region highlights the overlap range through which with decreasing k there is a transition from DRAO ST to GHIGLS data. Shown for comparison (Section 5.3) is the power spectrum of the scaled interferometric data alone (red, only for $k < 0.05 \text{ arcmin}^{-1}$).

tually falling off at low k , as in Figure 11. With the addition of the GHIGLS data the power-law rise in the power spectrum of the combined map extends to lower k (with no discontinuity as in Figure C.1). The power-law exponent found within the white dashed contour, -2.94 ± 0.02 , is consistent with that found for the white rectangle (-2.95 ± 0.03) and with those in Figures 11 and C.1.

The power spectrum shows that spatial fluctuations in the structure of the H I emission are smaller on small angular scales (high k) compared to those on large scales. Thus when the data are filtered to contain only those small scales, the amplitudes in the image domain are relatively small (and both positive and negative) as shown in the upper panel of Figure 13. In contrast to this, when the data are filtered to contain only large scales, the amplitudes in the image domain are relatively large as shown in the middle panel of Figure 13 (note the larger range on the colorbar).

We note that the high resolution filtered image has less dynamic range than the channel map of the DF-i mosaic in Figure 9, because the weighting applied to the $u-v$ data from the interferometer (Section 5.2) cuts off the power quickly across the overlap region toward lower k (see Figure B.1), thus removing the brighter fluctuations on the larger scales. Those fluctuations are captured in the low resolution filtered image. Likewise, the low resolution filtered image lacks the finer spatial detail in the original GHIGLS data, because the weighting applied cuts off faster than the effect of primary beam of the GBT (Figure B.1). A corollary is that the overlap in $u-v$ coverage of the DRAO ST and the GBT is so good that the spatial structure at scales covering the central part of the overlap range could equally well be represented by data of high quality derived from either instrument.

From the comparison in Figure 13 it can be appreciated that short-spacing “correction” is actually a contribution of fundamental importance, laying out the basic structure of the map, which the interferometric data adjusts to reveal the finer detail.

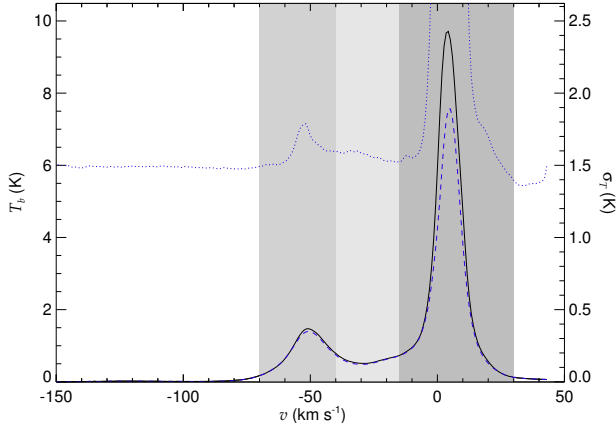


Figure 15. Spectral profiles within white dashed contour for the DHIGLS DF cube. Mean and median values of T_b (solid and dashed lines, respectively, left axis). Standard deviation about the mean of $T_b(v)$, σ_T (dotted line, right axis). From right to left the shaded bands indicate the velocity ranges of three velocity components: LVC and an exploratory subdivision of IVC into IVC1 and IVC2.

Table 2
Velocity Component Boundaries (km s⁻¹)

Name	LVC	IVC	HVC
<i>SPIDER</i> ^a	39.9	-14.9	-88.1
DF ^{ab}	30.0	-15.0	-70.0
<i>N1</i>	57.6	-10.8	-59.9
EN ^c	25.0	-30.0	-80.0
<i>G86</i>	23.8	-26.9	-64.8
MG	18.0	-15.0	-55.0
<i>DRACO</i>	23.8	-8.4	-72.8
DR	10.0	-12.0	-57.0
<i>POL</i>	31.8	-48.7	-97.0
PO	15.0	-8.0	-40.0
<i>POL</i>	31.8	-48.7	-97.0
MC	10.0	-9.0	-55.0
<i>UMA</i>	50.4	-26.1	-84.9
UM	15.0	-25.0	-65.0

^aPair of rows: first row for GHIGLS field (italics); second row for gas in DHIGLS region, a subset of the GHIGLS field.

^bIVC range subdivided in Figure 15.

^cRanges shown in Figure 16.

6. PROPERTIES OF DISTINCT VELOCITY COMPONENTS

6.1. Specification of VCs

Within the cube distinct velocity structures can be identified. To quantify the division of the cube into VCs, we computed the mean, median and standard deviation about the mean of each channel (see Figure 15), following the method in [Planck Collaboration XXIV \(2011\)](#) and [Martin et al. \(2015\)](#). Components often appear blended in the mean and median spectra, but become more distinct in the standard deviation spectrum, which depends on the fluctuations across the field, not just the presence of signal, and so takes advantage of the rich structure within the cube. Peaks in the standard deviation spectrum were noted and each was taken to indicate a separate velocity component. For DF, these are at about 3 km s⁻¹, -30 km s⁻¹ and -50 km s⁻¹. Minima at about -15 km s⁻¹ and -40 km s⁻¹ suggest velocities

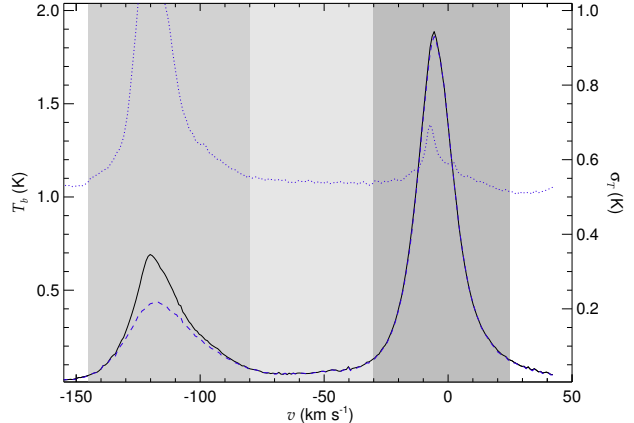


Figure 16. Spectral profiles as in Figure 15, for EN. There is no significant IVC in the area covered by the DRAO ST mosaic. LVC and HVC velocity ranges are indicated by the darker shading.

at which the cube can be divided into components. For exploratory purposes we divided the IVC range into two separate components, which we label IVC1 and IVC2. The separation here can be compared with the velocity cuts made in [Planck Collaboration XXIV \(2011\)](#) for the GHIGLS data in the SPIDER field (of which DF is a subset): LVC/IVC separation at -14.9 km s⁻¹ and IVC/HVC separation at -88.1 km s⁻¹ (see Table 2). Here there is no HVC component readily identifiable, unlike for the GHIGLS SPIDER field where the lower resolution provides higher sensitivity. Also, the coverage in DF does not fully overlap with the HVC seen in the GHIGLS SPIDER data, and where it does is along the noisy edge of the mosaicked region.

A second example is given in Figure 16 for EN. Results are tabulated in Table 2 along with those for the other DHIGLS regions and the corresponding GHIGLS fields identified in Table 1.

6.2. Maps of Column Density for VCs

The data cubes collapsed along their velocity axis produce maps of integrated emission, $W_{\text{HI}} = \sum_i T_b^i \Delta v$. The integrated emission is limited to channels where there is a measurable signal. An example of such a map is shown in Figure 17 for DF with emission integrated between -80 and +30 km s⁻¹ including both IVC and LVC (Figure 15).

The quantity W_{HI} is of particular interest because in the optically thin regime the column density $N_{\text{HI}} = C W_{\text{HI}} \text{ cm}^{-2}$, where $C = 0.1823 \times 10^{19} \text{ cm}^{-2} (\text{K km s}^{-1})^{-1}$. Although of some significance for the GHIGLS data, an optical depth correction might seem less important for the DHIGLS data presented here because they are noisier. Nonetheless, the correction is a systematic one and for consistent treatment of the data in both surveys an optical depth correction was made assuming a single spin temperature $T_s = 80 \text{ K}$ ([Martin et al. 2015](#)) in Equation (D1). The related issue of the dependence of optical depth corrections on the angular resolution of the observations is explored in Appendix D.1.

Some resulting N_{HI} maps produced from the DHIGLS HI cubes are shown in Figure 18 and Figure 19. Others for the remaining regions are included in Appendix F.

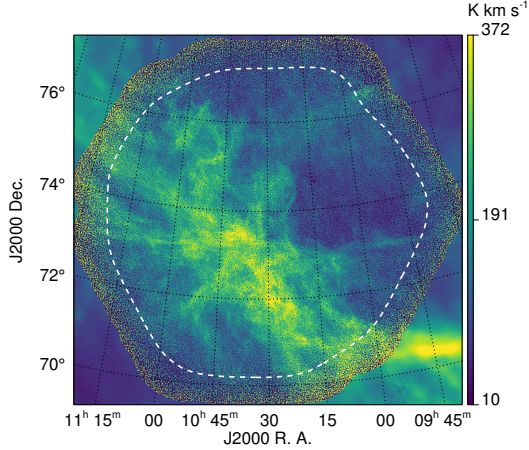


Figure 17. Integrated emission, W_{HI} , in DF. White dashed contour as in Figure 3. The area beyond where data have been combined has been filled in the cube using interpolated lower-resolution GHIGLS data (Section 5.2).

These N_{HI} products are available for download from the DHIGLS archive (see end of Section 9).

As presented in Appendix C.1 and discussed further in Section 7.2, the optimal S/N in an N_{HI} map is obtained by integrating only a few channels near the peak emission, about 10 in the case of DF. However, for the above N_{HI} maps of a full VC integration is carried out over many more channels to cover the range in which emission is seen anywhere in the map. Therefore, the N_{HI} maps in Figures 18 and F.3 clearly appear noisier than color maps based on single channels with strong emission (see Figures 24 and 25 below). The spectrum at each pixel could be integrated separately, keeping only data above some noise threshold, but unlike for the centroid velocity this would bias N_{HI} . Fitting Gaussian components and then integrating them over velocity is an alternative that accounts implicitly for noisy empty channels.

6.3. Maps of Centroid Velocity for VCs

On the basis of work on fractional Brownian motion (fBm) simulations, [Miville-Deschênes et al. \(2003b\)](#) suggested a direct mapping between the power spectrum of the centroid velocity map of a VC and the 3D velocity field. This motivated our computation of centroid velocity maps for all of the VCs in the DHIGLS regions. The DHIGLS cubes have not been filtered and so noise is a factor in determining a reliable centroid velocity power spectrum. In order to reduce some of this uncertainty, each spectrum in the cube is first filtered using a 5-channel-wide Hanning window (i.e., a Hanning function with 5 non-zero values). The centroid velocity field, v_c , is then determined using only those channels in the given component’s velocity range with signal above twice the emission-free end channel noise, σ_{ef} :

$$v_c = \frac{\sum_i v^i T_b^i \Delta v}{\sum_i T_b^i \Delta v} \quad ; \quad T_b^i > 2\sigma_{\text{ef}}. \quad (2)$$

Centroid velocity maps for DF, EN, and UM are shown in Figures 20, 21, and F.4, respectively. These images show structures on all scales and sometimes systematic gradients, most visible at large scales (e.g., the HVC in EN in Figure 21). The centroid velocity maps look some-

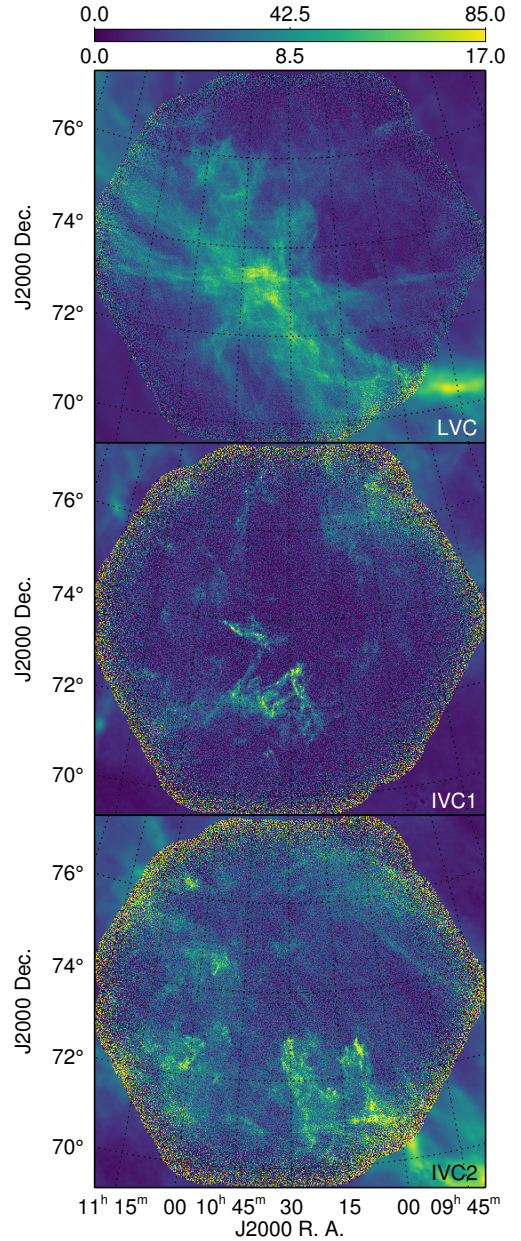


Figure 18. Maps of N_{HI} for DF VCs centered at (top to bottom): 7.5 km s^{-1} (LVC), -27.5 km s^{-1} (IVC1), and -55 km s^{-1} (IVC2) for velocity ranges in Figure 15. Colorbar for lower two N_{HI} maps scaled by a factor of 5. Units are 10^{19} cm^{-2} . Outer parts of the maps are filled in with GHIGLS data as in Figure 17.

what less noisy than the N_{HI} maps because of the spectral smoothing and clipping performed.

7. POWER SPECTRUM ANALYSIS OF H I STRUCTURE

7.1. Power Spectrum Analysis of Maps of N_{HI}

As described in Appendix A.2 we deconvolved the data with the appropriate 2D synthesized beam (Table 1) before computing the 1D power spectrum and fitting it with the model in Equation (A1). As in Appendix C.1 and Appendix A.4, we selected data within the non-rectangular white dashed contour. The model has three parameters to be fitted: the power law exponent, the amplitude normalization, and the scale factor of a noise

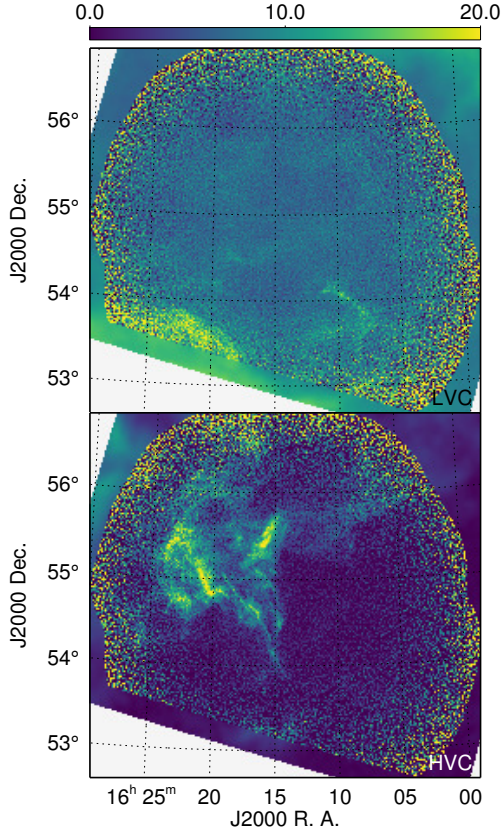


Figure 19. Like Figure 18, for EN VCs centered at -2.5 km s^{-1} (LVC, top) and -112.5 km s^{-1} (HVC, bottom) for velocity ranges in Figure 16 and Table 2 (no significant IVC emission in area covered by DRAO ST mosaic). Areas not covered by GHIGLS N1 survey are white.

template.

The power spectra of the N_{HI} maps of three VCs in DF (Figure 18) are shown in the upper panel of Figure 22, where it is readily apparent that the spectra for IVC1 and IVC2 are consistently shallower than for the LVC, indicative of *relatively* more power on smaller scales. This is quantified by the power-law fits, also shown in the figure. The power spectrum of the N_{HI} map of the combined IVC (Table 2) is similarly shallower. The exponents for LVC and IVC tabulated in Table 3 are significantly different. Fits to data within the more restricted white rectangle give consistent results within the uncertainties. We also note that while there are systematic uncertainties (< 0.1) in the derivation of the exponents, assessment of their relative differences is not impacted (Appendix A.3).

EN has very little IVC emission. Power spectra for the other two VCs (Figure 22, middle) indicate that the HVC spectrum is marginally steeper than that for the LVC. Additionally, the HVC exponent in Table 3 can be compared to the exponent for the rectangular field in the single EN-i HVC channel at -117.7 km s^{-1} used in Section 4.4, -2.21 ± 0.12 , or more appropriately here, the exponent for the same channel in the DHIGLS cube within the white dashed contour, -2.30 ± 0.09 . This suggests a steepening of the power spectrum with the inclusion of additional channels (see the discussion in Section 7.2).

The UM data are not as deep as in DF or EN, but nevertheless the H I signal in the power spectrum is well

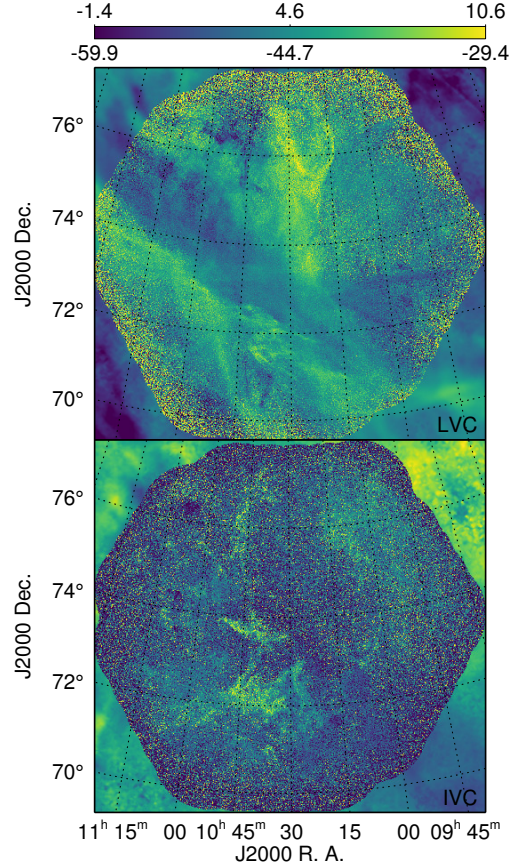


Figure 20. Centroid velocity maps for DF for VCs centered at 7.5 km s^{-1} (LVC, top) and -42.5 km s^{-1} (IVC including IVC1 and IVC2, bottom) for velocity ranges in Table 2. Units are km s^{-1} .

defined. For the N_{HI} maps of the LVC and IVC components (Figure F.3) we again found a steeper exponent for the LVC component (see Figure 22, lower, and Table 3). The value of the LVC VC is comparable to that for the single LVC channel value, -2.93 ± 0.08 , from Section 4.4 for the white rectangle region in Figure F.2. UM is immediately adjacent to and overlaps slightly DF (Figures 1 and 24) for which we found a similar pair of exponents for the LVC and IVC components (Table 3). We note that the UM-i mosaic contains a deeper observation of the URSA subregion for which a steeper power spectrum (exponent -3.6 ± 0.2) was found in previous work (Miville-Deschênes et al. 2003a). This is revisited in Appendix E.

Results for DR and PO are presented in Appendix F.

7.1.1. Comparison with Power Spectra of Thermal Dust Emission

Because dust and gas are well correlated in the intermediate latitude ISM (e.g., Planck Collaboration XXIV 2011; Planck Collaboration Int. XVII 2014), it is of interest to examine also the power spectra of dust maps to see how they compare with those from H I.

A dust map records all dust emission along the line of sight, independent of velocity. First, we compute a dust-proxy map from the combination of N_{HI} maps of the LVC and IVC weighted by the opacity $\tau_{\text{dust}}/N_{\text{HI}}$ for those two VCs (Planck Collaboration XXIV 2011). HVC is excluded because it is observed to have little

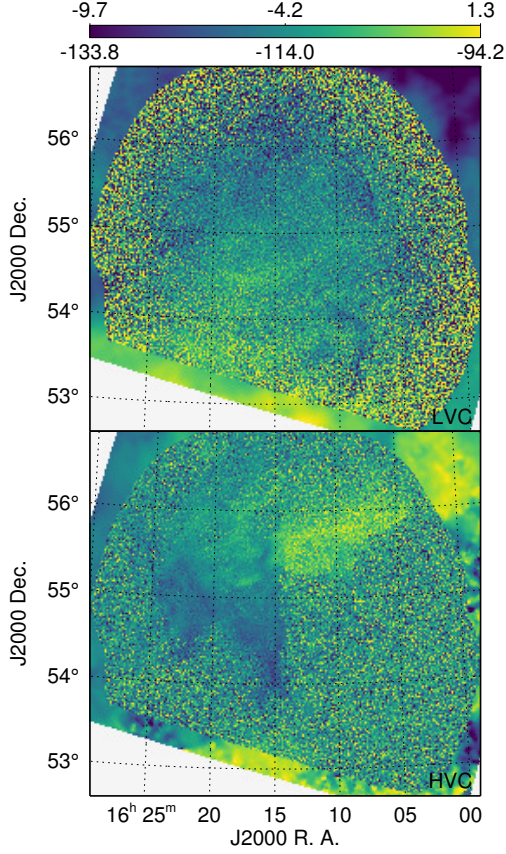


Figure 21. Like Figure 20, for EN VCs centered at -2.5 km s^{-1} (LVC, top) and -112.5 km s^{-1} (HVC, bottom) for velocity ranges in Figure 16 and Table 2.

Table 3
Power-law Model Results for DF, EN, and UM

Map	DF	EN	UM
LVC N_{HI}	-3.00 ± 0.03	-2.45 ± 0.17	-2.89 ± 0.04
v^a	-2.78 ± 0.08	-2.43 ± 0.16	-3.03 ± 0.09
IVC N_{HI}	-2.60 ± 0.04	...	-2.48 ± 0.06
v	-2.17 ± 0.10	...	-2.59 ± 0.15
HVC N_{HI}	...	-2.85 ± 0.07	...
v	...	-2.78 ± 0.30	...
H I, LVC+IVC ^b	-3.00 ± 0.04	-2.45 ± 0.17	-2.85 ± 0.04
$E(B-V)_{\text{xgal}}^{c,d}$	-2.69 ± 0.07	-1.55 ± 0.11	-2.66 ± 0.08
τ_{353}^c	-2.39 ± 0.08	-1.46 ± 0.15	-2.43 ± 0.08
857 GHz ^{c,d}	-2.64 ± 0.07	-1.19 ± 0.17	-2.52 ± 0.07
857 GHz ^c	-2.53 ± 0.07	-1.10 ± 0.19	-2.48 ± 0.08

^aCentroid velocity map

^bProxy for dust emission: combined N_{HI} components weighted by $\tau_{\text{dust}}/N_{\text{HI}}$ of the correlated dust components from [Planck Collaboration XXIV \(2011\)](#)

^cFrom [Planck Collaboration XI \(2014\)](#), 5' resolution

^dNo point sources

correlated far-IR or submillimeter emission. This proxy is expected to map the dust correlated with H I. A further consideration in these comparisons is that this proxy does not account for dust associated with molecular and/or ionized hydrogen. Exponents for this proxy are recorded in a central row of Table 3.

The thermal dust maps that we use for comparison are from the *Planck* thermal dust model as described

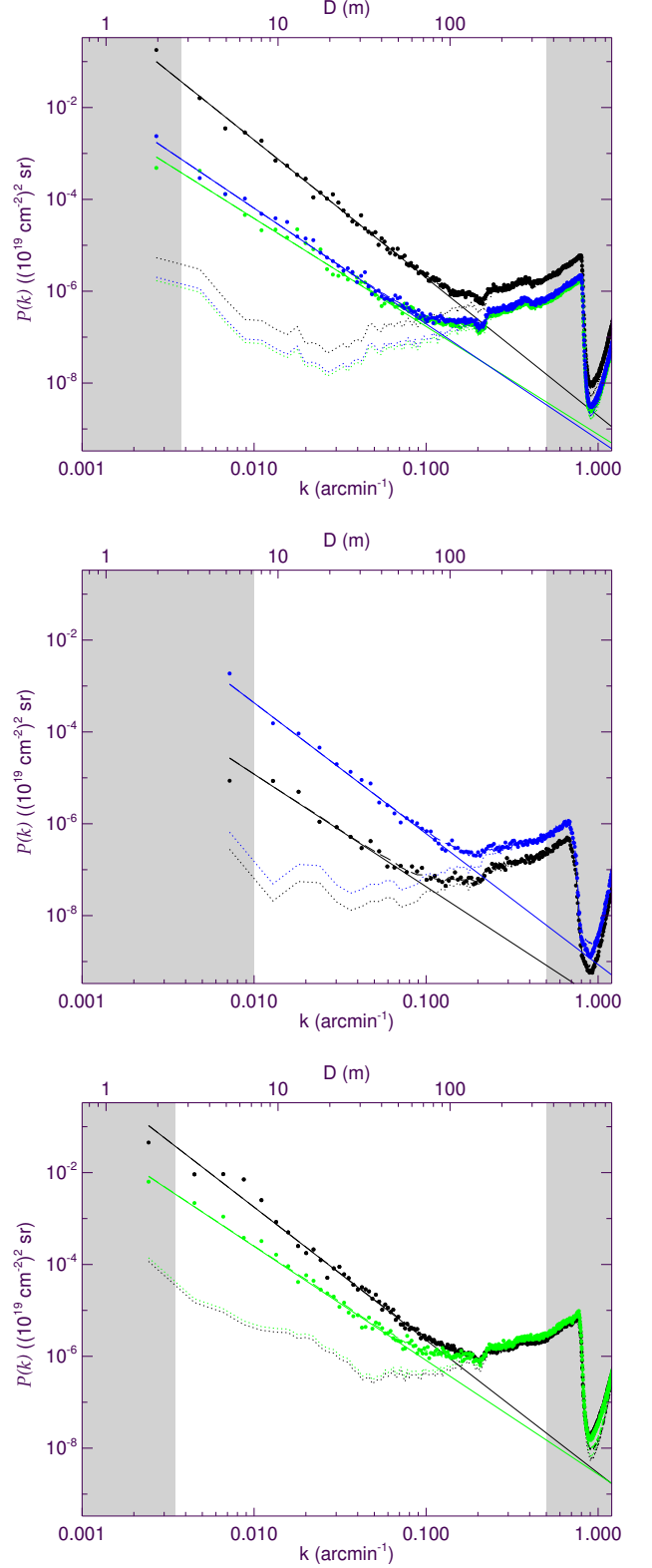


Figure 22. Power spectra for images of emission integrated over distinct velocity ranges. Upper: for DF for the ranges in Figure 18: LVC (black), IVC1 (green), and IVC2 (blue). Middle: for EN for the ranges in Figure 19: LVC (black) and HVC (blue). Lower: for UM for the ranges in Figure F.3: LVC (black) and IVC (green).

in [Planck Collaboration XI \(2014\)](#) and available on the Planck Legacy Archive.¹⁷ They have a 5' beam and a 1'7 grid. For the regions of interest here, the product most relevant for comparison with the dust proxy is $E(B-V)_{\text{Xgal}}$ scaled from the radiance derived using data with point sources removed. To assess systematic effects we also present results from maps of τ_{353} (dust optical depth at 353 GHz) from data including point sources and maps of the 857 GHz intensity used to determine the thermal dust model, both without and with point sources. The intensity maps relate to column density with further modulation by spatial variations in the dust temperature and in the exponent of the frequency dependency of the opacity.

For each of these dust maps, we selected regions corresponding to the DHIGLS white dashed contours, removing a median and applying an apodization, thus ensuring that all maps have the same masked area and edge-smoothing. The deconvolved power spectra of the DHIGLS dust-proxy maps were fit, as before, with a power law and scaled noise template. The power laws from thermal dust products were similarly fit, first deconvolving by the 5' beam. Our initial choice of a white noise model did not appear to apply to all cases. Instead we limited the fitted k -range to $k < 0.08 \text{ arcmin}^{-1}$, where the noise is significantly lower than the power law, eliminating the noise model from the fit altogether. From an empirical assessment of the effects of such adjustments to the fitting procedure, we deduce that there could be a systematic uncertainty of 0.1 in the exponent in comparison to that from analysis of the corresponding proxy N_{HI} map.

The results of the modelling the dust maps are summarized in the lower part of [Table 3](#). In DF, the exponents for the submillimeter dust products are reasonably consistent with that for the N_{HI} (LVC+IVC) dust proxy, although the latter power law appears marginally steeper. The results for UM are similar. On the other hand, there is a much more significant deviation relative to the exponent for the exponent for the dust proxy in the case of EN. This arises because this field is an ‘‘extragalactic window’’ and so has a very low column density of LVC ($\langle N_{\text{HI}} \rangle = 6 \times 10^{19} \text{ cm}^{-2}$) and correspondingly low Galactic dust emission. Fluctuations of the cosmic infrared background radiation, which have a power law exponent about -1 ([Planck Collaboration XXIV 2011](#)), seriously contaminate the dust maps, causing the flattening of the power spectrum (~ -1.5) in this specially selected region. Increasing the size of the dust maps of EN by a factor of 2, thus sampling brighter Galactic dust emission, results in a steeper power law with exponent -2.9 .

7.2. Dependence on Thickness: Velocity Channel Analysis

Angular power spectra of the ISM gas (and dust) such as discussed above reflect a self-similarity that has long been associated with a turbulent cascade ([Chandrasekhar 1949](#)). It is not necessarily straightforward to quantify all aspects of this turbulence directly from observations. For example, as seen in [Figure 24](#), the CNM structure in the channel maps changes quickly with velocity, but a channel map does not necessarily represent a slice of space/distance. Likewise a spatial slice need not

exhibit the same velocity throughout the map. In general the pattern of emission in individual channels in the H I velocity cube can reflect a combination of both the density and the velocity structure of the ISM. Attempts have been made to disentangle the effects of these two fields.

For optically thin gas, [Lazarian & Pogosyan \(2000\)](#) predict that for typical velocity field exponents the power law exponent of the integrated H I emission should decrease (the spectrum steepens) as the spatial thickness of the sampled region increases, approaching the power law exponent of the underlying 3D density field. The important condition is that the physical depth (δd) associated with the VC must exceed the largest transverse scale s of the map, which can be obtained from [Equation \(4\)](#) below. The intermediate Galactic latitude fields DF, UM, and EN span about 7° , 5° , and 2° , respectively. Adopting a distance of about 100 pc for the LVC in these fields, then from [Equation \(4\)](#) below the transverse extent s of the entire field would be of order 12, 8.5, and 3.5 pc, respectively.

In general, the LVC is composed of WNM, CNM, and thermally unstable components ([Saury et al. 2014](#)). The scale height of the WNM, $H_z \sim 400 \text{ pc}$ ([Kalberla 2003](#)), supporting the view that the range δd of gas contributing to the integrated column density significantly exceeds s for intermediate-latitude LVC gas over regions of the size observed in DHIGLS. Furthermore, CNM is thought to form within the WNM via a thermal phase transition. There is a pressure threshold for this transition and so δd might be somewhat smaller for the CNM. Nevertheless, the spatially-thick condition $\delta d > s$ seems likely to be met here. This in turn suggests that the measured LVC power laws (-3.00 ± 0.03 , -2.45 ± 0.17 , -2.89 ± 0.04 in row 1 of [Table 3](#)) represent the 3D density power spectrum of the H I gas.

Using fBm simulations, [Miville-Deschênes et al. \(2003b\)](#) found that increasing the number of LVC channels being integrated does indeed steepen the power law as the relative contribution of power on the smallest scales is reduced. They find that the exponent decreases by of order unity and interpret this phenomenon as a measure of the change from 2D to 3D in the captured topology.

The large velocity range needed to capture a ‘‘complete’’ VC could often be associated with a large thickness, although as discussed velocity does not map uniquely to distance. To explore such potential variations in the power spectra of the data, we started with the channel map with peak emission in the standard deviation spectrum (e.g., [Figure 15](#)) and added channels around these peaks, on alternating sides, eventually building up component maps as in [Figures 18 and 19](#). At each step we used the model in [Equation \(A1\)](#) to determine the power-law exponent. As the number of channels in the slice integrated increases, the S/N first increases and then decreases. Estimating the relative S/N as a function of the slice width by P_0/η with $k_0 = 0.01 \text{ arcmin}^{-1}$ we found the width at which the S/N was at a maximum.

The trend lines in [Figure 23](#) show the results for DF for the three velocity ranges identified in [Figure 15](#). The exponents for IVC1 and IVC2 are similar to one another

¹⁷ <http://www.cosmos.esa.int/web/planck/pla/>.

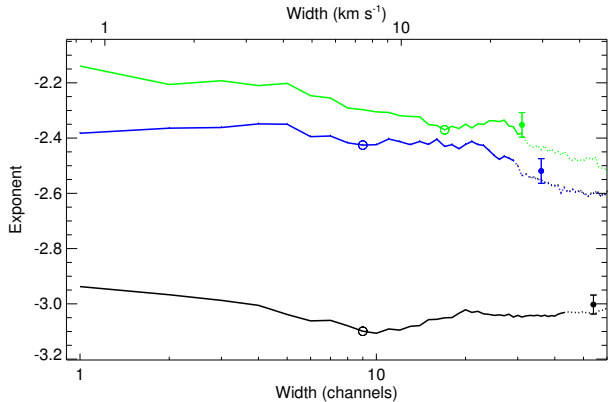


Figure 23. Modelled power-law exponents as a function of width of the velocity slice for DF emission within the LVC, IVC1, and IVC2 ranges. Velocity slices are centered at 3.0 km s^{-1} (black), -27.5 km s^{-1} (green), and -52.0 km s^{-1} (blue), respectively (Figure 15). Trend line is solid where gas is entirely within the range of the VC. Filled circle, for exponent found fitting the complete VC (Figure 22), falls slightly off the trend line at the same width, because the slice centers and centers of the VC velocity ranges do not quite coincide. Unfilled circle indicates exponent for the velocity slice for which S/N of power spectrum is maximum.

but different than for LVC. We also marked the exponent for the slice width at which the S/N was maximum and plotted the exponents found in the power spectrum analysis of N_{HI} of the complete VCs (Figure 22).

Our main result is that there is no significant decrease in the exponent with width of the slice (a possible surrogate for spatial thickness). This is the case for EN and UM as well and in contrast to a decrease of the exponent with slice width by 0.45 found by Miville-Deschênes et al. (2003a) in URSA (see also Appendix E). However, for the HVC in EN there appears to be a steepening of the power spectrum with the inclusion of additional channels, from exponent -2.30 ± 0.09 for a single channel to -2.85 ± 0.07 for the full VC, which is in the sense expected from theory and simulations.

7.3. Geometrical Effects Relating to Distance

Given the angular extent of DF, UM, and EN, the power spectrum samples well down to about k of 0.005, 0.007, and 0.02 arcmin^{-1} , respectively. At the other extreme, the S/N is sufficient in each underlying mosaic to probe the power spectrum readily up to k of about 0.2 arcmin^{-1} , corresponding to a scale of $5'$, somewhat larger than the synthesized beam.

For an adopted distance of LVC gas of 100 pc, the DHIGLS data probe down to scales of 0.14 pc and up to 10 pc in the case of DF and UM.

The IVC, on the other hand, might lie in the more distant Galactic halo, say 1 kpc. The power spectrum in that case would be probing transverse scales about 10 times larger, perhaps up to 100 pc in the case of DF and UM. Noting that the transition from probing 3D to probing 2D turbulence occurs when $\delta d < s$ (here, $s \sim 100 \text{ pc}$), the relatively shallow spectra seen for the IVC VCs might indicate that these data are probing such a 2D topology, in which case the observed exponent would depend on the exponent of the velocity field as well (also relatively shallow, see Section 7.4). However, not much is known about the depth of the IVC. A typical IVC

column density is $3 \times 10^{19} \text{ cm}^{-2}$ and so volume density $n_{\text{HI}} = 0.1 \text{ cm}^{-3}$ would translate to depths of 100 pc using Equation (3) below. In Section 8 we present evidence for significant CNM in the IVC that would indicate higher n_{HI} and lower depths within these structures. However, the relevant δd is the amount by which gas across the region is spread out along the line of sight, not the depth of individual features.

The Draco nebula, estimated to be at a distance of about 500 pc (Gladders et al. 1998), is an interesting IVC because it shows an interaction with the embedding Galactic halo (Section 8.1, Miville-Deschênes et al. 2016). In the interaction region the gas has become dense enough to be molecular, and so the depth there might be of order a pc, smaller than the angular extent of 15 pc. The power spectrum is again relatively shallow (-2.68 ± 0.07 , Appendix F.2), perhaps suggestive of a 2D topology, but δd across the region is not readily known. Alternatively a shallower behaviour compared to typical LVC might simply reflect different conditions in the driving of the turbulence in the two components.

The HVC gas in N1 is part of Complex C at an estimated distance of $\sim 10 \pm 0.3 \text{ kpc}$ (Thom et al. 2008). Adopting this distance, the power spectrum would be probing transverse scales up to 300 pc for the 2° EN field. The power spectrum exponent is not atypical, and so if revealing a 3D topology would imply $\delta d > 300 \text{ pc}$ and a mean density $< 0.01 \text{ cm}^{-3}$. From the line profiles, it appears that the HVC component could be divided into a broad (WNM-like) and narrow (CNM-like) component. The narrow-line components are quite compact, some about $3'$ or 10 pc at the adopted distance. These individual features have N_{HI} about $7 \times 10^{19} \text{ cm}^{-2}$ and so a typical n_{HI} of 3 cm^{-3} , perhaps greater locally if clumpy below the beam scale. This is much larger than the average density, but does not necessarily imply $\delta d < s$ because again the relevant δd is the amount by which the gas, including the condensed structures (filaments, nuggets), is spread out along the line of sight. Furthermore, the turbulent conditions in this infalling gas could be quite different from Galactic LVC gas, making interpretation more challenging.

7.4. Power Spectra of Maps of Centroid Velocity

We also analysed the centroid velocity maps for all VCs in DF, EN, and UM (Figures 20, 21, and F.4, respectively), with the goal of determining the power spectrum of the 3D velocity field (Miville-Deschênes et al. 2003b). To quantify the power spectrum the centroid velocity data were deconvolved by the DRAO ST beam and modelled with a power law. Interestingly, the noise component at high k is similar to the noise template used for the N_{HI} power spectrum models up to $k \sim 0.8$; however, the shape is not as consistent and so we chose to fit a power law model without a noise template. This precludes the use of high k power in the model fit, limiting the range to $k < 0.06 \text{ arcmin}^{-1}$. An associated systematic uncertainty in the exponent in comparison to analysis of N_{HI} maps of the same VC could amount to 0.1.

As summarized in Table 3, the power law exponents for the centroid velocity maps are for the most part the same as those found for the N_{HI} maps, within the uncertainties. This interesting empirical result is not a general ex-

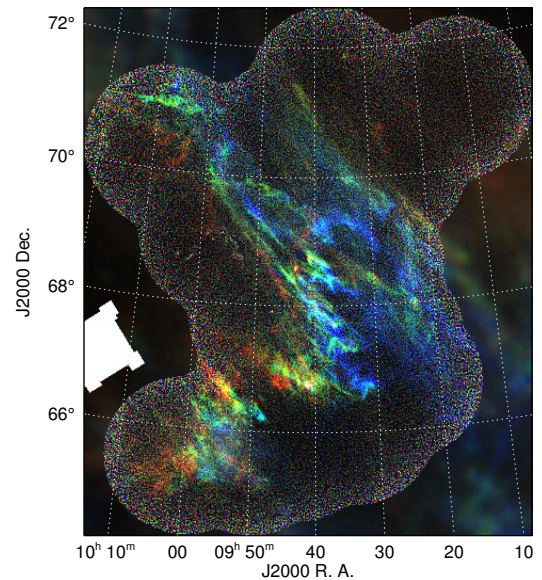
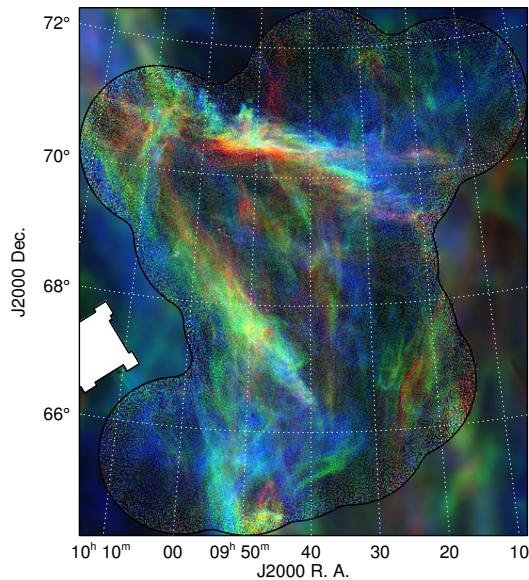
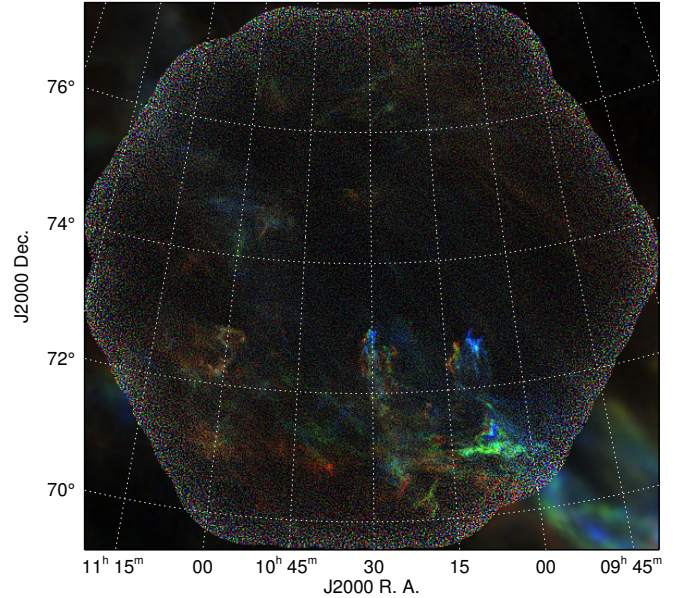
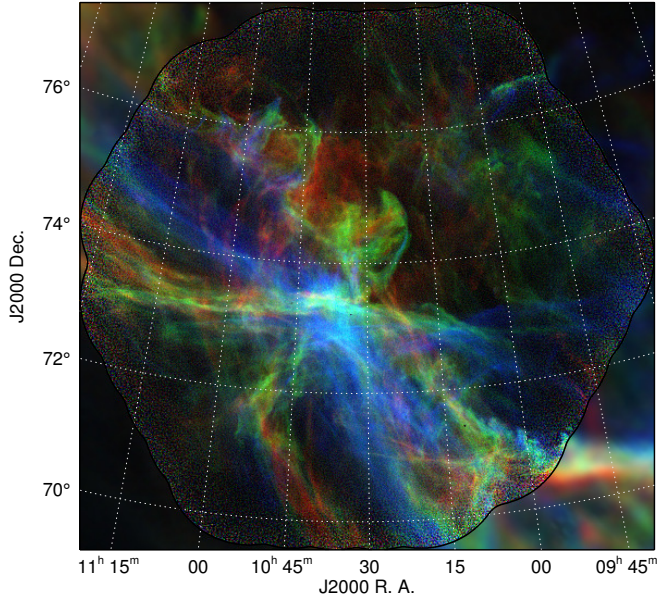


Figure 24. Illustration of dramatic changes in channel maps with velocity in DF (upper) and UM (lower). RGB images were made using three distinct LVC channels from the cubes at 7.59 km s^{-1} (red), 5.12 km s^{-1} (green), and 2.64 km s^{-1} (blue); for each color the identical intensity range was used, from 0 K (black) to 40 K (color saturation). Upper left portion of UM image joins onto lower right of DF image (see also Figure 1). In parts of the overlap the different angular resolutions of the DHIGLS and the GHIGLS data can be appreciated (a black curve separates the two).

pectation of theory and implies that the 3D velocity field and the 3D density field (see discussion in Section 7.2) have rather similar statistical properties. An exception might be the centroid velocity map of DF IVC, which being a combination of IVC1 and IVC2 with distinct velocities and spatial structure is more complex.

8. STRUCTURES ASSOCIATED WITH NARROW EMISSION AND ABSORPTION LINES

For the intermediate latitude lines of sight targeted, the DHIGLS data reveal the distribution of H I in un-

Figure 25. Similar to Figure 24 but for IVC channels with intensity extremes at 0 K and 15 K because the IVC emission is fainter. The three distinct channels used from the cubes were at -49.28 km s^{-1} (red), -51.76 km s^{-1} (green), and -54.23 km s^{-1} (blue).

precedented detail, to sub-pc scales for the LVC gas. In this section we provide a glimpse of this rich information to encourage further exploration of the cubes. The empirical relationship of the diffuse H I emission and the fine structure in both intensity and velocity should provide valuable insight into the neutral atomic component of the multiphase ISM (Cox 2005; Wolfire 2015) when combined with relevant numerical modelling incorporating the essential physics of the turbulent magnetized interstellar medium (e.g., Bryan et al. 2014; Dobbs et al. 2014; Hennebelle & Iffrig 2014; Kim et al. 2014; Kim & Ostriker 2015) and including the influence of dynamics on the transition to molecular hydrogen (Sternberg et al. 2014; Valdivia et al. 2016). Likewise, the new dynami-

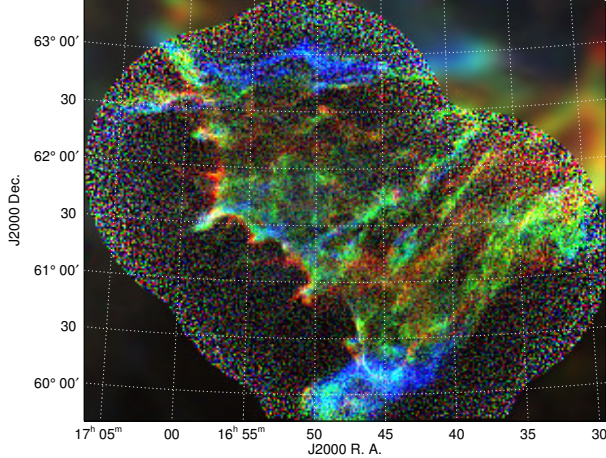


Figure 26. Similar to Figure 24, for DR IVC channels with intensity extremes at 0 K and 15 K as for the IVC in Figure 25. The three distinct channels used from the cube were at -19.61 km s^{-1} (red), -22.08 km s^{-1} (green), and -24.56 km s^{-1} (blue).

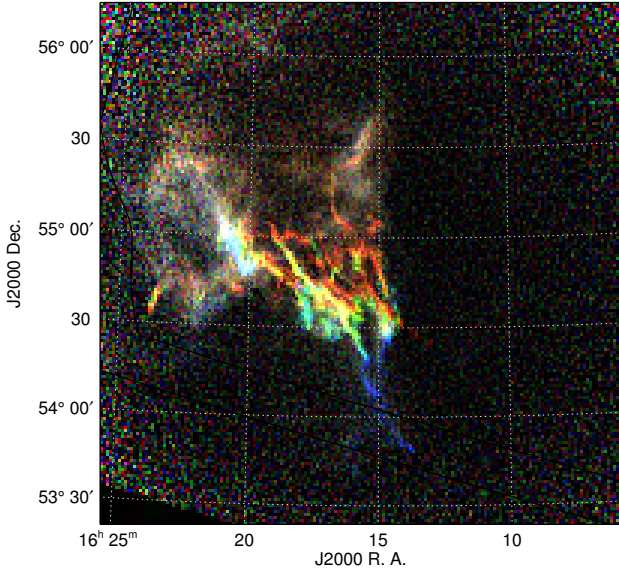


Figure 27. Similar to Figure 24, for EN HVC channels with intensity extremes at 0 K and only 5 K because the HVC emission is relatively weak. The three distinct channels used from the cube were at $-120.17 \text{ km s}^{-1}$ (red), $-122.64 \text{ km s}^{-1}$ (green), and $-125.12 \text{ km s}^{-1}$ (blue).

cal information illustrated on the interaction of IVC and HVC gas in the Galactic halo should provide important constraints for accurate numerical models of these phenomena in 3D (e.g., Heitsch & Putman 2009; Schneider & Robertson 2015).

8.1. Structure in Channel Maps

Examination of the H I data cubes shows that the structure in the channel maps changes dramatically over even small changes of velocity. At the spatial positions of these distinctive structures, the line profiles have significant narrow components. To illustrate this we made RGB color images of the H I emission using three distinct channels offset by 2.47 km s^{-1} . Examples are given for

a variety of environments: LVC gas in the overlapping DF and UM regions in the NCPL (Figure 24); IVC gas in these same regions (Figure 25) and in DR (the Draco nebula, Figure 26); and HVC gas in EN (Figure 27).

For each figure, the intensity ranges for the channels represented by different primary colors are identical. Therefore, when the line profiles are sufficiently narrow and the emission at different velocities does not overlap spatially, the image appears red, green, or blue. With partial overlap at similar intensity, the image appears yellow or cyan (other blending possibilities resulting in magenta or white are rare in these examples).

The channel offset used, 2.47 km s^{-1} , corresponds to the FWHM of a thermally broadened H I line at a kinetic temperature of about 130 K, even without allowance for instrumental and turbulent broadening. The fine structure that appears in a single colour in this visualization comes from narrow line components of CNM gas, as can be corroborated by independent estimates of the density and spin temperature of the gas (Sections 8.2 and 8.3).

The LVC H I seen in Figure 24 has a turbulent and filamentary nature; angular power spectra of single channel maps are illustrated in Figures 11, 12, and 14.

In the IVC range the channel maps of DF and UM near -50 km s^{-1} (Figure 25) have a streaky appearance, suggestive of a preferred orientation for the structures (approximately along constant Galactic latitude). Another distinguishing feature, compared with the appearance in the LVC range, is higher contrast frothy small-scale structure, also seen in PO near -21 km s^{-1} (Figure F.8). These maps have slightly flatter power spectra (see Figure 12 and also Figure 22 and Table 3). Power spectral analysis for images with such exceptional directional structure is discussed in Appendix A.5.

The color image of the Draco nebula, the IVC in DR (Figure 26), reveals some particularly interesting features. Relative to a diagonal running north east to south west (upper left to lower right) there is IVC gas to the upper right and a void, at those velocities, to the lower left. It has been suggested that infalling higher velocity gas is interacting with more tenuous gas at high altitude in the Galactic disk (Goerigk et al. 1983). The DHIGLS observations show the complexity of this interaction. Nevertheless, there are some important systematics that will be important to model. For example, in the central portion along this boundary there is a change in the characteristic velocity of the narrow line emission across the “leading edge,” from red to green (in radial motion approaching more quickly) in Figure 26 on an arc minute (0.15 pc) scale, as one passes from lower left to upper right. Along this edge the density is enhanced locally to the extent that CO is present and detectable in the *Planck* CO maps (Planck Collaboration XIII 2014). The corrugated structure of the edge might result from hydrodynamic instability in the interaction region (Miville-Deschênes et al. 2016).

In EN the LVC has no prominent small-scale structure except for a filament at -7 km s^{-1} at $16^{\text{h}}10^{\text{m}}, +54^{\circ}10'$; this filament was studied earlier with the GBT (Miville-Deschênes & Martin 2007) and is seen much more clearly in our DHIGLS data with the DRAO ST resolution. By contrast, the HVC image in Figure 27 reveals an intricate pattern of coherent narrow ribbons of emission at

Table 4

Parameters of select structures and derived volume density

Feature	Distance (pc)	FWHM (km s ⁻¹)	T_p (K)	ψ (')	n_{HI} (cm ⁻³)
DFa	100-200 ^a	4	20	15-30	30-120
DFb	100-200 ^a	3	4	4	40
ENa	150 ^b	4	10	6	100
ENb	10000 ^c	4	15	3	4

^aNCPL LVC distance, [Meyerdierks et al. \(1991\)](#)^bLVC distance, [Miville-Deschênes & Martin \(2007\)](#)^cHVC distance, [Thom et al. \(2008\)](#)

each particular velocity, with the structure in this velocity range shifting systematically with increasingly negative velocity to the lower right, along the general direction of the ribbons. The HVC gas in EN is part of Complex C at an estimated distance of $\sim 10 \pm 2.5$ kpc ([Thom et al. 2008](#)).

8.2. Volume Density

It is useful to check that the volume density in these structures is relatively high, as would be expected in the CNM as compared to the WNM.

If a column density N_{HI} arises in a physical depth δd , then the volume density n_{HI} is given by¹⁸

$$n_{\text{HI}} = 3.2 \frac{N_{\text{HI}}}{[10^{19} \text{ cm}^{-2}]} \frac{[1 \text{ pc}]}{\delta d} \text{ cm}^{-3}. \quad (3)$$

A structure of angular size ψ at distance d has a transverse size

$$s = 0.29 \frac{\psi}{[10']} \frac{d}{[100 \text{ pc}]} \text{ pc}. \quad (4)$$

Supposing that δd can be estimated from the narrowest dimension of the structure, ψ_n , then

$$n_{\text{HI}} = 11 \frac{N_{\text{HI}}}{[10^{19} \text{ cm}^{-2}]} \frac{[10']}{\psi_n} \frac{[100 \text{ pc}]}{d} \text{ cm}^{-3}. \quad (5)$$

For an optically thin H I line component approximated by a Gaussian specified by its peak brightness temperature T_p and FWHM,

$$\frac{N_{\text{HI}}}{[10^{19} \text{ cm}^{-2}]} = 16 \frac{T_p}{[20 \text{ K}]} \frac{\text{FWHM}}{[4 \text{ km s}^{-1}]}, \quad (6)$$

and

$$n_{\text{HI}} = 174 \frac{T_p}{[20 \text{ K}]} \frac{\text{FWHM}}{[4 \text{ km s}^{-1}]} \frac{[10']}{\psi_n} \frac{[100 \text{ pc}]}{d} \text{ cm}^{-3}. \quad (7)$$

Parameters and derived volume densities for a few worked examples are presented in Table 4. Consider first the green ‘‘face’’ and filaments in DF (Figure 24, upper), which we tabulate as DFa. From Equation (7), we find a volume density in the range $n_{\text{HI}} \sim 30 - 120 \text{ cm}^{-3}$, somewhat denser than the conditions for CNM gas modelled in [Wolfire et al. \(2003\)](#).

DF also hosts some remarkably long narrow structures. Among these, in the left hand side of channel maps near 9 km s^{-1} , is one (DFb) that runs over 3° along $\delta \sim +73.5$ but is barely resolved by the DRAO ST

¹⁸ Quantities in square brackets define the units of the parameters in the ratios in the following equations and are chosen so that the ratios are not too far from unity.

Table 5Parameters^a of select absorption features and derived T_s

Region	NVSS Source	T_c	v_{LSR}	T_n	T_b	T_s
DF	J101132 + 712440	380	+5.1	-70	25	84
UM	J094912 + 661459	444	+2.6	-106	25	85
UM	J094912 + 661459	444	-53.0	-58	13	80
DR	J164829 + 600722	41	-23.7	+5	18	55

^aVelocity in km s^{-1} and temperatures in K

synthesized beam, indicating an axial ratio of over 100. From the parameters in Table 4, $n_{\text{HI}} \sim 40 \text{ cm}^{-3}$ if it is indeed a filament in 3D.

Likewise, for the above-mentioned LVC filament in EN (ENa), we find $n_{\text{HI}} \sim 100 \text{ cm}^{-3}$.

The HVC ribbons seen in EN are neutral condensed structures with a density much higher than the estimated average, $n_{\text{HI}} \sim 0.03 \text{ cm}^{-3}$ ([Thom et al. 2008](#)), with a low covering factor. Furthermore, there is clear substructure along the ribbons. The brightest such nugget (ENb) at $16^{\text{h}}20^{\text{m}}37^{\text{s}}, +54^\circ55'25''$ in the -125 km s^{-1} channel map, has $n_{\text{HI}} \sim 4 \text{ cm}^{-3}$. The integrated column density of even this brightest nugget is still quite low, $N_{\text{HI}} \sim 10^{20} \text{ cm}^{-2}$ from Equation (6), requiring the angular resolution and sensitivity of the DHIGLS product to bring out the fine detail across the region.

8.3. Spin Temperature from Absorption against Radio Galaxies

H I absorption of bright background radio sources (e.g., [Roy et al. 2013](#); [Murray et al. 2015](#)) can be found in DHIGLS spectra. The absorption coefficient of H I varies inversely with spin temperature T_s , favouring the detection of cold gas.

Thanks to the relatively small size of the synthesized beam (θ_{sb} in arc seconds in Table 1) some radio point sources are detected with high continuum brightness temperatures T_c . For a source of flux density S_ν ,

$$T_c = 170 \left(\frac{[60'']}{\theta_{\text{sb}}} \right)^2 \frac{S_\nu}{[1 \text{ Jy}]} \text{ K}. \quad (8)$$

H I absorption reduces this background emission to $T_c \exp(-\tau)$. Because of continuum removal in the processing of the spectra, this results in a negative-going feature in the spectrum, of depth τT_c for small optical depth.

When τ is small, the net temperature T_n recorded in the DHIGLS spectrum is therefore

$$T_n = T_b(1 - T_c/T_s), \quad (9)$$

which becomes negative when $T_c > T_s$ or $S_\nu > 0.4 \text{ Jy}$ for $T_s = 80 \text{ K}$. From the NVSS catalog browser¹⁹ we find about 0.25 such sources per square degree and although this is small we have found instances of favorable alignments producing the expected narrow absorption features.²⁰

In DF a prominent example is 4C +71.09 (NVSS J101132+712440) which can be seen as a dark dot against emission at 5.12 km s^{-1} (green) in Figure 24 (upper).

¹⁹ <http://www.cv.nrao.edu/nvss/NVSSlist.shtml>

²⁰ We also note that fitting the position and angular extent of the absorption features in channel maps where they are prominent confirms the registration of the mosaics and expected size of θ_{sb} .

For this source, $T_c = 380$ K. The spectrum is most negative at 5.94 km s^{-1} with $T_n = -70$ K. The FWHM of the absorption feature is about 3.5 km s^{-1} . T_b interpolated spatially in the channel map is 25 K, with about 20 K attributable to narrow emission of FWHM 4 km s^{-1} , slightly broader than the absorption. Rearranging Equation (9), the spin temperature can be estimated from

$$T_s = T_c T_b / (T_b - T_n). \quad (10)$$

For this example, using the numbers collected in Table 5, this evaluates to $T_s = 84$ K and confirms that the optical depth is appropriately small (< 0.25) and that this is CNM gas as suggested above on the basis of n_{HI} . That the line width is slightly broader than thermal is usually attributed to turbulence, which also appears to play a role in the pressure distribution (Wolfire 2015).

There are many more examples of absorption indicating cold CNM gas in the LVC range. In UM, 4C +66.09 (NVSS J094912 + 661459) can be seen deeply absorbed at 2.64 km s^{-1} (blue in Figure 24, lower) with FWHM about 3.8 km s^{-1} as for nearby emission. Using the values in Table 5, $T_s = 85$ K.

Although lines of sight to bright radio sources rarely intersect sufficiently bright IVC gas, which has a lower covering factor than the LVC gas, there are a few examples in the DHIGLS data. Toward 4C +66.09 in UM the deepest absorption in the IVC range is at -53.0 km s^{-1} (cyan in Figure 25, lower), with FWHM about 3 km s^{-1} (absorption and emission). In this IVC feature, $T_s = 80$ K. Using $\psi_n \sim 10'$ and taking $d < 500$ pc, we find $n_{\text{HI}} > 20 \text{ cm}^{-3}$. Thus the IVC gas that reveals the frothy and streaky structure across the whole region is dense like CNM gas.

In DR, absorption of the weaker source NVSS J164829 + 600722 still produces a relative deficit visible in the -23.7 km s^{-1} emission (cyan) in Figure 26 and we find $T_s \sim 55$ K. This gas is part of the prominent higher column density region in the south which is molecular (Herbstmeier et al. 1993).

For the HVC range, because of factors like insufficient spectral coverage, faintness of emission, and low covering factor, there are no examples of absorption in DHIGLS data.

9. SUMMARY

We report on high resolution ($\sim 1'$) H I data from the DRAO ST acquired to complement the low resolution GHIGLS data from the GBT (Martin et al. 2015) and higher resolution dust emission data such as are available from *Herschel*/SPIRE surveys and *Planck*. The DHIGLS data probe intermediate-latitude gas of moderate column density over several distinct velocity components comprising local gas in the Galactic disk, the ‘‘Galactic fountain,’’ and infalling H I from outside the Galaxy.

Following calibration of all of the DRAO ST data to a common NVSS scale using point sources in each field, an additional single cross calibration factor is found to adjust DRAO ST data to the GHIGLS scale. Thanks to the sensitivity and resolution of the GHIGLS data, this factor can be found from a direct comparison of the Fourier transformed data in the region where the spatial

frequencies of the two instruments overlap.²¹ The cross calibration factor is 1.12. This enables an accurate combination of the short-spacing information from GHIGLS with the interferometric DRAO ST data to produce the DHIGLS products. Disregarding this adjustment would result in artificially steep power spectra in the combined data.

We present a power spectrum analysis of the H I structure, based first on maps of integrated emission or column density N_{HI} for several distinct ranges of velocity. In the analysis we make use of a power law model of the H I signal in combination with models of the noise and of the effects of the synthesized beam at high spatial frequencies. For the four large regions incorporating many DRAO ST pointings, we find a range in power spectrum exponents from -2.5 to -3.0 , with IVC tending to lie toward the shallower end and LVC somewhat steeper. The HVC gas is well characterized in the EN region and has an exponent toward the high end of this range. For LVC gas, increasing the number of channels integrated to form the N_{HI} map, from one to the number defining a full velocity component, does not produce any large (i.e., order unity) decrease of the power law exponents. These results and trends are complemented by a power spectrum analysis of the centroid velocity maps of these components, which implies that the 3D velocity field and the 3D density field have similar statistical properties.

The DHIGLS regions contain distinctive structure at low, intermediate, and high velocities down to the resolvable scale. Illustrative figures are provided that demonstrate that this structure can change dramatically even over a few channels. This can be appreciated in the movies of the data cubes on the DHIGLS archive as well. Estimates of the volume density associated with this narrow-line emission are relatively high, consistent with this gas being in the phase called the CNM. Where this can be probed using absorption against background radio galaxies, the spin temperature is found to be low, again typical of CNM gas. Examples of absorption are found in the LVC and IVC ranges. Because of several conspiring factors, there are no examples of absorption in the HVC range in the DHIGLS data.

A digital archive at www.cita.utoronto.ca/DHIGLS contains the DHIGLS H I data cubes and derived products. On the digital archive the FITS data cube for each region has extensions as follows: 0, the cube of spectra, T_b in K; 1, the modified weight map (closely related to the noise map, Section 4.2) of the DRAO ST mosaicked data (e.g., Figure 7 bottom), set to zero to indicate the area in which the data are simply the lower-resolution GHIGLS data, not the new DHIGLS product (Section 5.2); and 2, a mask carried over from the GHIGLS data recording the few pixels in that data with no baseline fit removed from the spectrum (DHIGLS data could be interpolated to replace these spectra if necessary). For a preview of the H I structure in the cube, we provide a movie showing successive channel maps over the entire velocity range. We also include FITS cubes whose planes are N_{HI} maps ($T_s = 80$ K) for different velocity VCs (see Table 2). The standard deviation spectra used to choose the velocity ranges, as in Figure 15, are

²¹ As described in Appendix B this combination of facilities is unique in the significant overlap in spatial frequency.

presented as well.

ACKNOWLEDGMENTS

We acknowledge support from the Natural Sciences and Engineering Research Council (NSERC) of Canada and thank the DRAO staff for their outstanding support of this ambitious project. We also thank the referee for constructive comments that have led to improvements in the presentation of our results.

APPENDIX

A. IMPLEMENTATION OF POWER SPECTRUM ANALYSIS

Here we provide details of how we computed the power spectrum and extracted quantitative information, building on work described in Miville-Deschênes et al. (2007) and Martin et al. (2015).

In practice in computing the 2D power spectrum, $P(k_x, k_y)$ (Equation (1)), we first altered the image $f(x, y)$ by subtracting the median and then apodizing using a cosine function along its rectangular boundary. These both reduce edge effects inherent to any Fourier transform of a finite nonperiodic function, which otherwise would appear as excess power along the $u = 0$ and $v = 0$ axes (Miville-Deschênes et al. 2002). Apodization in the image plane over five pixels at each edge is normally sufficient to suppress this “centered cross” in $P(k_x, k_y)$ in the u - v domain, but even after apodization the potential artificial cross should be monitored and if necessary masked in 2D. For the collapsed 1D power spectrum, notionally formed by azimuthal averaging, taking the median rather than the average is an effective complement to apodization and mitigation against any residual cross, and to be conservative we adopted that strategy.

Because of the asymmetry of the synthesized beam (Table 1), we chose to deconvolve the power spectrum moduli in 2D in the u - v domain before calculating the 1D power spectrum, distinguished as $P_d(k)$.

Figure 11 shows the 1D power spectrum for the H I channel map in Figure 9 for DF-i, with and without deconvolution.

A.1. Power Spectrum of the Noise

The noise in a mosaic made using the interferometric data from the DRAO ST is quite complex. The spectral noise is not uniform over the map (see example in upper panel of Figure 7). The power spectrum of an emission-free channel is not flat (see example in Figure 11) but it has a consistent shape and scale for a given mosaic. For example, at values of k corresponding to antenna spacings of $34L$ to $38L$ ($D \sim 146$ to 163 m or $k \sim 0.20$ to 0.22 arcmin $^{-1}$), the noise is slightly reduced because the strategy for the separation of the moveable antennas and their discrete movements results in twice as much coverage at these antenna spacings. This can be seen clearly in the power spectrum of the emission-free channel in Figure 11. At higher values of k the desired H I signal is being reduced by the synthesized beam and this example shows how, even in relatively bright intermediate Galactic latitude regions like DF, the noise dominates at large k . As described in Section 3, a Gaussian taper was applied in the Fourier domain, apodizing the visibilities

at high k . In Figure 11 it can be seen how this taper has affected the level and shape of the power spectrum of the noise above $k = 0.4$ arcmin $^{-1}$.

We exploit the consistent shape to calculate a median of the 2D power spectra for a set of emission-free channels for each mosaic. We call this the “noise template.” After deconvolution by the relevant beam, we form the 1D equivalent, $N_d(k)$. At high k this is greatly amplified compared to the version without deconvolution, $N(k)$. Because the noise is always larger when there is an H I signal (e.g., Martin et al. 2015), this template needs to be scaled by a fitting factor $\eta > 1$, as in Equations (A2) and (A1) below.

A.2. Power Spectrum Models

The 1D power spectrum of deconvolved data can be described with a parameterized model consisting of a power law representation of the signal plus a noise component:

$$P_{\text{model,d}}(k) = P_0 (k/k_0)^\gamma + \eta N_d(k), \quad (\text{A1})$$

where P_0 is the amplitude of the power law at some representative scale k_0 and γ is the scaling exponent. The exponent is alternatively called the spectral index or the slope (in a log–log representation).

Without deconvolution, the original data are modified by the effective beam decreased at high k through $\tilde{\phi}^2(k)$ so that the model would be

$$P_{\text{model}}(k) = \tilde{\phi}^2(k) P_0 (k/k_0)^\gamma + \eta N(k). \quad (\text{A2})$$

For application in the above 1D model the effective $\tilde{\phi}^2(k)$ can be estimated directly from the 1D power spectrum formed from the 2D power spectrum of a representative synthesized beam at the center of the DRAO ST mosaic. As a check, fitting such a 1D power spectrum with a Gaussian results in equivalent 1D Gaussian beams for DF and EN that have quite similar FWHM, $56''.8 \pm 0''.7$ and $58''.9 \pm 0''.9$, respectively, both reasonably consistent with the 2D Gaussian beam statistics as summarized in Table 1.

Example power spectra of signal and noise are shown in Figure 11 for the DF-i mosaic. Generally a noise template is calculated from many emission-free channels (Appendix A.1). In this example for simplicity the noise template is from a single representative emission-free channel ($v = 39.7$ km s $^{-1}$, as also used in Figure 2, left).

A.3. Fitting the Power Spectrum

We adopt the model represented by Equation (A1) to probe the power spectrum of the signal to smaller spatial scales while properly accounting for the noise.

We also mitigated against further uncertainty in model fits by excluding data above a value k_{max} ; the results below are not sensitive to the precise value so long as the noise can be adequately assessed. We adopted 0.5 arcmin $^{-1}$ (which corresponds to baselines of 361 m).

In the DRAO ST observations there are no data corresponding to spacings shorter than 13 m and so there is little power at $k < 0.018$ arcmin $^{-1}$ except from foreshortened baselines. This is reflected in the power spectrum of the signal in Figure 11, where there is a precipitous departure below the rising power law at 0.018 arcmin $^{-1}$. The remedy for this is to add short-spacing data acquired

with a large single antenna (Section 5). For the power spectrum fits to the DRAO ST data alone, we excluded data below a value k_{\min} , here taken to be $0.018 \text{ arcmin}^{-1}$.

The three best-fit model parameters were found using the IDL routine `mpfit.pro` (Markwardt 2009), with the described uncertainties as weights. The weights were further modified at high k using the prescription in Martin et al. (2015), specifically substituting fractional error $b = 0.07$ into their Equation (4) to account for the uncertainty of the effect of the beam.

The fits to the models for DF-i data are shown in Figure 11 in Section 4.4. The exponent is $\gamma = -3.03 \pm 0.03$. The uncertainties that we cite are the formal 1σ errors from the fits. Alternative choices in the fitting analysis could lead to systematic uncertainties in the exponent, which we estimate to be no larger than 0.1. We also found that relative differences between the exponents for different channels or VCs (Section 7.1) are robust against the systematic effects.

A.4. Power Spectra of Non-Rectangular Regions

Apodizing a (median-subtracted) map prior to computing the Fourier transform has the benefit of reducing edge effects. Normally maps can be made rectangular and so only a simple rectangular taper is required. The unique shapes of the DHIGLS regions are distinctly non-rectangular. One alternative is to define an inscribed rectangle, as we have done, but this inevitably leaves out high signal to noise data. This led us to an alternative approach aimed at incorporating as much spatial information from each mosaic as possible, in this case using data within the white dashed contour (e.g., Figure 3).

We modified the shape of the taper so that rather than following a straight edge of the map it followed a contour of constant weight (or noise) in the DRAO ST mosaic. The median-subtracted maps were tapered to zero orthogonal to the chosen contour. The $35'$ taper was centred on the contour. These tapered maps were then cropped to a rectangular map aligned with the zeroed edges of the map. Because of the unique shapes of the DHIGLS regions, information is missing between the zeroed edges of the map and the boundary of the rectangle; this was padded with zeroes. In practice the 2D taper was obtained by convolving a unit mask defined by the contour with a circularly-symmetric tapering function of the desired shape and width and then cropping.

The drawback of any tapering (apodization) of the map is that the resulting Fourier transform has also been modified: the true Fourier transform has been convolved with the Fourier transform of the taper. The Fourier transforms of the various non-rectangular zero-padded apodization functions obtained as described above are all centrally-peaked, suggesting that a convolution in the Fourier domain will not have a significant effect on the measured power law exponent of the original DHIGLS map. (The amplitude is affected, but that is not of interest here.)

We have tested this conjecture using simulations. Fractional Brownian motion (fBm) maps were created with a given power law exponent (Miville-Deschênes et al. 2003b). We apodized these maps with the custom-shaped DHIGLS taper, Fourier transformed them, and computed the power spectrum. Each power spectrum was then modelled to find the power law exponent. We

found that the results were consistent with those used to make the fBm maps within the model uncertainties.

A.5. Power Spectra in 2D

Implicit in the construction of the power spectrum in 1D is that the 2D power spectrum is azimuthally symmetric. For exceptional images with a pronounced streaky appearance, the directionality affects the 2D power spectrum. For example, for the single channel of IVC emission in the UM region at -51.76 km s^{-1} , seen in green in Figure 25, lower, the directionality of the structure is roughly on the upper-left to lower-right diagonal, and in the image of the 2D power spectrum there is more power in the $u-v$ plane orthogonal to this, roughly in two opposed quadrants. This can be brought out most effectively in the image by removing the radial dependence, i.e., by dividing the 2D power spectrum by the model fit to the 1D power spectrum, which has exponent -2.35 ± 0.03 .

To quantify what is seen visually, as a simple approximation we made a 1D power spectrum by azimuthally averaging within these opposed quadrants, and another 1D power spectrum for the other two complementary quadrants. The power law exponents were quite similar (-2.28 ± 0.04 and -2.27 ± 0.05 , respectively). Thus the systematic effect is apparently not large. However, as expected the amplitudes were different, in this case by a factor of about 2. Given the similar exponents, it is not surprising that the amplitude for the overall 1D power spectrum is close to the mean of the amplitudes for the two separate 1D power spectra.

We are often interested in power spectra of images of integrated emission, N_{HI} (Section 7.1). Because the H I structure changes over many channels, the directionality is less pronounced in N_{HI} (e.g., compare Figures 25 and F.3), so that forming the 1D power spectrum is more suitable and less prone to systematic effects. For the case above, recall that the exponent for the somewhat noisier N_{HI} image of the full IVC VC in UM was -2.48 ± 0.06 (Table 3).

Also, in comparing the power spectra of images of two independent tracers, for example N_{HI} and thermal dust (Section 7.1.1), it seems likely that any systematic effects will be similar given a common directionality.

B. RANGES IN THE $u-v$ DOMAIN FOR ADDING SHORT-SPACING DATA

As discussed in Section 5, an essential step in wide-field imaging with interferometers is addition of short-spacing data from a single dish. In Figure B.1 we summarize information relevant to the $u-v$ ranges available and adopted in cross calibrating and combining the data sets in DHIGLS and in previous H I surveys: the CGPS (Landecker et al. 2000; Taylor et al. 2003; Higgs et al. 2005), VGPS (Stil et al. 2006), and SGPS (McClure-Griffiths et al. 2005).

Each combination of survey facilities is characterized by two beams, one for the synthesized (restored) beam, extending to higher k , and one for the single dish. The curves of $B(k)$ in Figure B.1 show how the visibilities in the $u-v$ domain are diminished by the beam. The cutoff from the single dish beam and the presence of noise clearly limit the $u-v$ range for overlapping data at the high- k end. Near the low- k end, vertical lines rep-

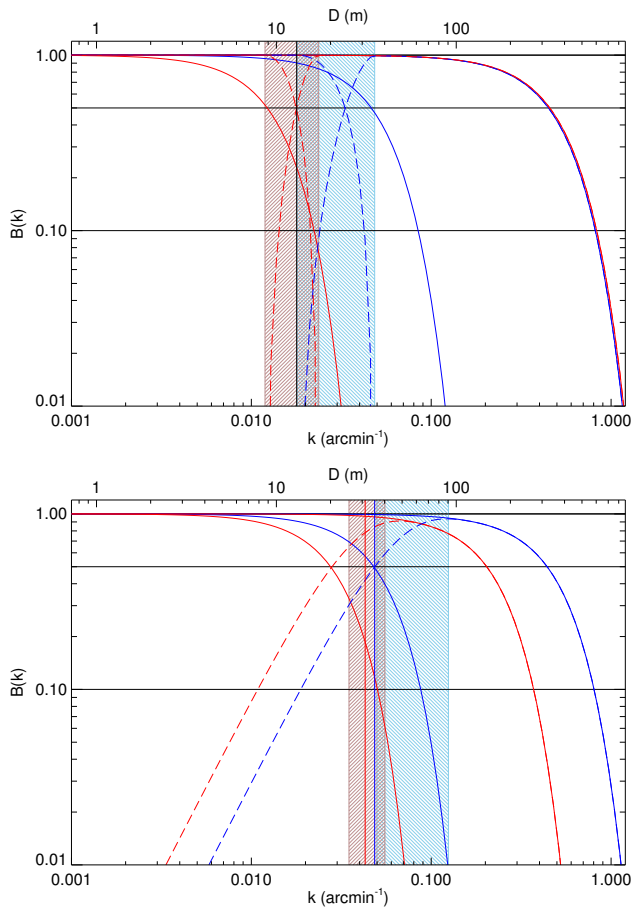


Figure B.1. Beams $B(k)$ in the Fourier domain for the interferometers (synthesized/restored beams: solid curves on right extending to higher k) and for the single dishes used to supply the short-spacing H I data (solid curves on left). Curves, each represented as a Gaussian, show how visibilities in the $u-v$ domain are diminished by the beam. Vertical line indicates shortest unprojected baseline of the interferometer. These considerations are relevant to the $u-v$ ranges adopted for cross calibration of data sets (shaded). They are also relevant for combining data; the complementary weighting functions of $u-v$ data (dashed curves) cross at 0.5. For DHIGLS see Appendix C.2 and Section 5.2, respectively. Upper: CGPS (red) and DHIGLS (blue) both use the DRAO ST but incorporate different single dish data, from DRAO 26 m and GBT 100 m, respectively. Lower: SGPS (red) combining ATCA and Parkes 64 m and VGPS (blue) combining VLA and GBT 100 m. In both of these surveys the feathering of the single dish data follows the beam profile and the combination range spans all k .

represent the minimum unprojected baseline in the interferometer. This does not take into account foreshortening or mosaicking. A counter-consideration relating to foreshortening of the shortest baseline is shadowing for compact configurations and low elevation observations. The shaded regions in Figure B.1 show the baseline ranges used in cross calibrating the data.

In combining the two data sets, in the case of the DRAO ST the deconvolved single dish $u-v$ data are used below the lower bound of this range and the interferometric data above the upper bound. At intermediate k in between, they are combined after weighting in the Fourier domain using the complementary functions shown as dashed curves in the upper panel of Figure B.1. In the case of the SGPS and VGPS one of the weighting functions used for the combination of data is defined by the single dish beam (therefore not appearing as dashed

in the lower panel of Figure B.1), in effect reversing the deconvolution of that data set; this and the complementary weighting function define a combination range spanning a range in k much broader than the range used for cross calibration.

B.1. Reflections on Choices for Different H I Surveys

CGPS (Figure B.1, upper, red). Short-spacing data were added for each separate synthesis before mosaicking. For the single dish data, the 26 m is quite undersized for the task. The lower bound adopted is lower than the minimum baseline (8.6 m versus 12.9 m; see Higgs et al. 2005). Even so, the single dish data needed in the overlap range are well down in the 26 m beam.

SGPS (lower, red). The Parkes 64 m beam is also cutting off data significantly over the entire overlap range. This was mitigated somewhat by mosaicking of the ATCA data (McClure-Griffiths et al. 2005), which reduces the effective minimum baseline by $D/2$, where D is the diameter of the antennas making up the interferometer. Still the feathering implies an extrapolation of the interferometric data to low k . The reduction by the synthesized beam is barely relevant.

VGPS (lower, blue). The minimum baseline of the VLA is quite large (36 m), so that the overlap range is affected by the beam of the GBT despite its 100 m aperture. The lower and upper bounds adopted for cross calibration (not given in Stil et al. 2006) were 36 m and 90 m (Jeroen Stil, private communication).

DHIGLS(upper, blue). The mosaicking by SUPERTILE was not designed to achieve the $D/2$ reduction in minimum baseline. Still, relative to the facilities combined in other surveys, there is a potentially much broader $u-v$ overlap range because the minimum baseline is small, the GBT is large, and the synthesized beam is small. Relative noise is also a consideration. Details are given in Section 5.

C. GHIGLS AND DRAO ST CROSS CALIBRATION

Here we describe the evaluation of the scale factor, $f_{cc} \equiv I_{GBT}/I_{DRAO}$, required for the accurate combination of the mosaics made from the DRAO ST data with the lower resolution single dish GHIGLS data. Note that this factor is the inverse of that used by the MIRIAD (Sault et al. 1995) task IMMERGE, which corrects short-spacing data to the scale of the interferometric data.

C.1. Preparation of the Data

The cross calibration comparison was done at the lower resolution of the GHIGLS data and in the $u-v$ domain. The evaluation of f_{cc} was carried out optimally using the full 2D information.

We used the data for the DF region to refine our approach, as illustrated below. The GHIGLS SPIDER data are in the Galactic GLS projection whereas the DF-i mosaic is in the ICRS NCP projection. To minimize reprocessing of the GHIGLS data and to ensure the same spatial coverage for the cross calibration, the DF-i cube was reprojected to the same Galactic GLS projection as the GHIGLS data, adopting the same $18''$ pixel grid spacing as in the original DF-i cube. We also processed the weight map in the same way, to track the region in which the two data sets could be compared, and similarly the

synthesized beam map. The velocity channels were interpolated to correspond to those in the SPIDER cube.

For the cross calibration the signal needs to stand out from the noise. With regard to the noise, we compared the data in the region where the noise level in the DF-i mosaic is no more than a factor of two larger than the noise minimum (see the white dashed contour in Figure 3). With regard to the signal, we compared the data near the peak in the LVC H I spectrum. Specifically, we used a map of W_{HI} , the integral of the H I spectra, including only N_{ch} channels near the peak of the H I standard deviation spectrum (see Figure 15). We estimated the relative signal-to-noise ratio (S/N) as a function of N_{ch} using $W_{\text{sd}}/\sqrt{N_{\text{ch}}}$, where W_{sd} is the standard deviation about the mean (alternatively it can be estimated via analysis of the power spectrum). We adopted the range $1.6 \text{ km s}^{-1} < v_{\text{LSR}} < 6.5 \text{ km s}^{-1}$ to create the optimal W_{HI} map, which results in a S/N about twice that of a single channel.

As in Appendix A.4, starting with the original GHIGLS data in the image plane we first removed the median value of the data (in this case W_{HI}) within the white dashed contour, then apodized with a $35'$ taper centered on the contour to reduce the data to zero, and beyond that in the encompassing square image padded with zeros. We then computed the 2D Fourier transform $\hat{f}(k_x, k_y)$ of this modified image. The tapering and padding with zeroes, applied equally to two fields to be compared, will not affect the derived scale factor. As discussed in Appendix A.4, there is no significant effect on the power law exponent either. We note that this scheme is similar to that used by Bertincourt et al. (2016) for power spectra of non-rectangular regions in the determination of a cross calibration factor for *Herschel*/SPIRE and *Planck*/HFI data.

To produce the corresponding product for the DRAO ST data, starting with W_{HI} from the finely-gridded reprojected DF-i data described above, we deconvolved with the synthesized beam, convolved with the 2D GHIGLS beam, and regridded to the coarser GHIGLS image grid. We then selected the region, removed the median, apodized, and zero-padded in the same way as for the GHIGLS data, and finally computed the 2D Fourier transform.

Solely for visualizing the relative calibration of the data we also produced another closely related product from the DRAO ST image data, omitting the steps of convolving with the 2D GHIGLS beam and regridding to the coarser GHIGLS image grid. As in Appendix A we computed the 1D power spectrum from these 2D data and from those for GHIGLS. Figure C.1 shows the power spectra of the two data products and the power law fits calculated for the different but overlapping k ranges appropriate to the two data sets. The power spectrum exponent for the GHIGLS data, -3.00 ± 0.05 , is very close to that for the DRAO ST data, -3.06 ± 0.03 . This is an important check that has not been possible for the other H I surveys mentioned. Furthermore, it is clear that a vertical shift is required to align the DRAO ST data with those from the GBT data. The amount of the shift is f_{cc}^2 .

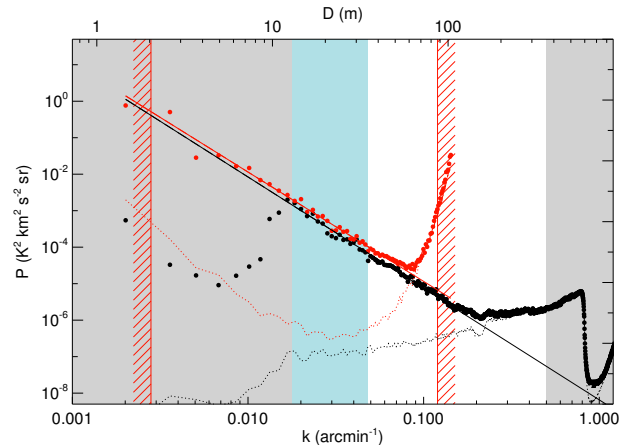


Figure C.1. Power spectra for the DF region for spectral data integrated over channels near the peak in the standard deviation spectrum (see text). Deconvolved DRAO ST data shown in black and GHIGLS GBT data shown in red. DRAO ST power spectrum is fit to Equation (A1) as for single channel case in Figure 11. Fit to the GHIGLS power spectrum follows same model, but with a different noise template and a different range in k as indicated by vertical hatched regions in red. Blue band identifies overlapping range of k used for cross calibration, well outside influence of noise in the GHIGLS data and any uncertainties in the GHIGLS beam.

C.2. The Overlap Range

Next we consider the “overlap range” in k , or in practice an annulus in the $u-v$ domain, in which the data are to be compared.

On the low side this range is constrained by the minimum baseline of the interferometer. As above for the DRAO ST we chose 13 m ($0.018 \text{ arcmin}^{-1}$). This is a conservatively higher choice relative to the minimum baseline, compared to other H I surveys (Figure B.1). Nevertheless, it is still not far into the range of k that is affected by the beam of the (short-spacing) single dish data, as was necessary for the VGPS (larger minimum baseline), CGPS (smaller single dishes), or SGPS (combination of the two).

The choice for the high- k side depends on properties of the GBT data. It needs to take into account the relative noise of the two data sets, which can be assessed using power spectrum model fits according to Equation (A1). As is apparent from the results shown in Figure C.1, because of the effect of the GHIGLS beam, as we move to higher values of k in the power spectrum, the GBT noise becomes larger relative to not only the DRAO ST noise but also the H I signal. Another consideration is that data in the entire range of k being considered are affected by the GHIGLS beam, and any uncertainties in the beam would produce more pronounced effects at higher values of k (the synthesized beam is not a consideration). To be conservative, we adopted 35 m ($0.0485 \text{ arcmin}^{-1}$).

Despite these conservative choices, the overlap range is relatively broad and much less impacted by the beam of the single dish data as compared to the other surveys (Figure B.1); this provides the opportunity for a more critical assessment of the cross calibration determination.

C.3. Quantitative Comparisons of the Data

There are a number of different methods for determining the cross calibration factor. The one we adopted, as in IMMERGE, was to correlate the complex 2D Fourier

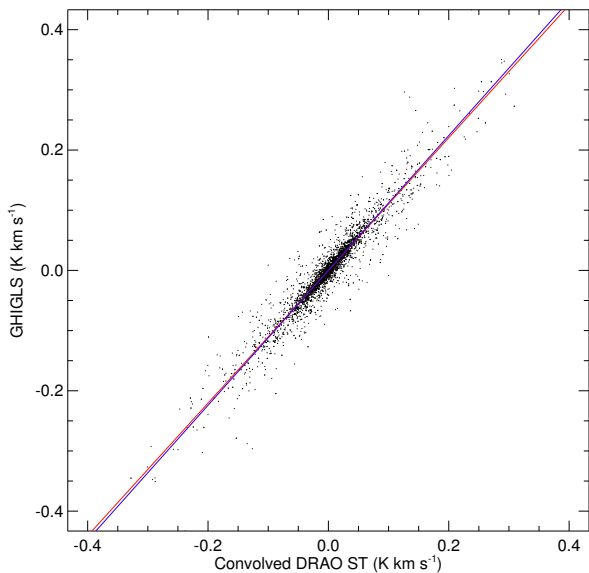


Figure C.2. Correlation of complex Fourier-transformed data (real and imaginary parts are kept distinct and plotted separately) in annulus in u - v domain corresponding to overlapping k range, illustrated for DF integrated spectral data used in Figure C.1. Blue line shows the least absolute deviation fit, with slope $I_{\text{GBT}}/I_{\text{DRAOST}} = 1.12 \pm 0.01$ (for systematic uncertainties, see text). Red line, from ordinary least squares fit, is very similar (slope 1.10 ± 0.01).

transformed data (keeping real and imaginary parts distinct) within the overlap-range annulus in the u - v domain. To mitigate against any residual cross, we masked two rectangular regions each with a width of three pixels centered along each axis (i.e., along $u = 0$ and $v = 0$). The intercept from this correlation is consistent with zero within its error (Figure C.2) and subsequently in fitting the data we enforced this by adding data at $(0, 0)$ explicitly.

As judged from the noise power spectra, the GHIGLS data have greater uncertainty than those from the DRAO ST. This is confirmed by the standard deviation of the values of the modulus in rings of constant k . Therefore, we performed the usual “y on x” regression implied by the format of Figure C.2. As in IMMERGE, for the linear fit we minimized the absolute deviation (L1-norm). For the DF field we found $f_{\text{cc}} = 1.12 \pm 0.01$. We also used ordinary least squares fitting (i.e., minimizing the L2-norm), finding 1.10 ± 0.01 . Furthermore, the bisector slope is also the same within 1σ . These checks reinforce that the result is robust.

In the same way we found independent values of f_{cc} for four other regions, EN, UM, DR, and PO (see Table C.1). The DRAO ST syntheses included in these mosaics had different values of $F_{\text{DRAO}}/F_{\text{NVSS}}$ applied, indicating the efficacy of that part of the calibration.

C.4. Systematic Errors

We have investigated the systematic errors that might arise. One is from the choice of overlap range. For example, the values of f_{cc} using data from the independent annuli between 13 m and 26.4 m and between 26.4 m and 35 m are 1.09 ± 0.01 and 1.16 ± 0.01 , respectively.

Table C.1

Values of cross calibration scale factor $f_{\text{cc}} = I_{\text{GBT}}/I_{\text{DRAO}}$

Region	f_{cc}
DF	1.12 ± 0.01
EN	1.10 ± 0.02
UM	1.09 ± 0.01
DR	1.12 ± 0.02
PO	1.17 ± 0.02

Deconvolving the GHIGLS data and not convolving the DRAO ST data with the GHIGLS beam changes the effective weighting going into the slope. We found $f_{\text{cc}} = 1.13 \pm 0.01$.

We investigated correlating values of the Fourier amplitude (modulus of the visibility) in 2D. This again changes the weighting. We also note that at higher k the amplitudes are smaller but there are more independent data samples. We found $f_{\text{cc}} = 1.14 \pm 0.01$.

We also correlated power spectrum moduli in 2D, finding f_{cc} from the square root of the slope. This is akin to fitting a common power law to the two sets of data. Again the weighting changes and we found $f_{\text{cc}} = 1.12 \pm 0.01$. We note that correlating power spectrum moduli in 1D (a weighted fit is indicated) is less satisfactory, because of the compression of the data in k and azimuthal coverage before the correlation (though it should make no difference for noise-free data).

From these investigations, we estimate that the systematic error in f_{cc} is 0.03.

We also looked at the cross calibration factor synthesis by synthesis. The DRAO ST data have to be corrected for the effect of the primary beam, which limits the spatial coverage to about $90'$ and makes the data noisier at the low end of the k range. An annulus between 25 and 50 m ($0.034 < k < 0.069 \text{ arcmin}^{-1}$) was selected. We found a mean cross calibration factor 1.13 ± 0.01 , consistent with the above. As another check, we used DRAO ST data that were not scaled to NVSS and found that the values of $I_{\text{GBT}}/I_{\text{DRAO}}$ were well correlated with the inverse of $F_{\text{DRAO}}/F_{\text{NVSS}}$ (Section 3.5). This indicates that if cross calibration synthesis by synthesis were sufficiently precise, there would be no point in first doing the synthesis by synthesis scaling to NVSS.

We adopted a common cross calibration factor of $1.12 \pm 0.01 \pm 0.03$ for all seven DHIGLS regions. A correction of the same order was found by Pidopryhora et al. (2015) for combining GBT and VLA data. This is mentioned not for direct comparison to our f_{cc} , but to point out that a non-unity cross calibration factor is not unprecedented.

D. ESTIMATED OPTICAL DEPTH CORRECTIONS

It is generally the case for the DHIGLS spectra that the H I optical depth τ is small. This can be illustrated as follows. For optically thick H I emission, the brightness temperature T_{b} saturates at the spin temperature T_{s} . For optically thin emission, on the other hand, $T_{\text{b}} = \tau T_{\text{s}}$. A plausible value of the CNM spin temperature is $T_{\text{s}} = 80 \text{ K}$, the collisional temperature found from intermediate-latitude H_2 observations for values of N_{HI} near 10^{20} cm^{-2} (Gillmon et al. 2006; Wakker 2006). This is not too different from the distribution $67 \pm 14 \text{ K}$ found by Rachford et al. (2009) for translucent lines of sight at lower latitude. A single T_{s} along any line of

sight is in any case only an approximation. For CNM gas in thermal equilibrium [Wolfire et al. \(2003\)](#) show (in their Figure 10) that the gas temperature (and so T_s) is roughly inversely related to n_{HI} . For comparison to T_s , even for the channel map in DF with the brightest emission (at 3.45 km s^{-1}) the average T_b is 12 K; the dispersion is 9 K with a low exponential tail to about 40 K. The total emission is enhanced by contributions from the WNM gas as well, for which the absorption is much smaller. We conclude that optical depth effects on the H I emission spectrum are typically small.

Column density can be calculated with an approximate correction for optical depth assuming a single spin temperature T_s using

$$N_{\text{HI}} = C T_s \int -\ln \left(1 - \frac{T_b}{T_s} \right) dv \quad (\text{D1})$$

rather than simply $C W_{\text{HI}}$. We used $T_s = 80 \text{ K}$. Corrections are small, consistent with the results of [Lee et al. \(2015\)](#) for the Perseus molecular cloud region; they found significant corrections only for column densities much greater than $40 \times 10^{19} \text{ cm}^{-2}$, larger than typically found in our intermediate latitude regions.

D.1. Resolution Dependence

The correction in Equation (D1) clearly depends on the contrast of the observed brightness T_b relative to T_s . Because peaks in the intrinsic H I emission on the sky are diminished if the observing beam is larger than the spatial structure, the estimated optical depth correction is reduced at lower resolution.

We estimated the impact on GHIGLS N_{HI} maps by comparing results from data at two differing resolutions, assuming $T_s = 80 \text{ K}$. For the first map, N_{HI} was created from the DHIGLS cube using Equation (D1) and then convolved to the GHIGLS resolution and regridded to $3/5$ pixels. We call this $N_{\text{HI}}(\text{DHIGLS})$. For the second map we convolved the DHIGLS cube to the GHIGLS resolution, regridded, and then computed N_{HI} . We call this $N_{\text{HI}}(\text{GHIGLS})$. The resulting difference, expressed as $\Delta = N_{\text{HI}}(\text{DHIGLS})/C - N_{\text{HI}}(\text{GHIGLS})/C$, is positive.

Within the high signal to noise region bounded by the white dashed contour in DF, and for the LVC component, we found $\log(\Delta) = 0.02 \pm 0.2$ for Δ in units of K km s^{-1} , meaning that at the lower resolution of actual GHIGLS N_{HI}/C is underestimated by of order 0 to 2 K km s^{-1} for this region. From Table 3 in [Martin et al. \(2015\)](#), the uncertainty for the LVC component of (GHIGLS field) SPIDER, $\sigma_{N_{\text{HI}}} = 0.3 \times 10^{19} \text{ cm}^{-2}$, or $\sigma_{N_{\text{HI}}/C} \sim 2 \text{ K km s}^{-1}$, comparable to the maximum additional Δ correction. Thus the uncertainty of N_{HI} cited in [Martin et al. \(2015\)](#) might be somewhat underestimated in this systematic way by not accounting for the resolution dependence of optical depth effects. Further discussion of the effect of the optical depth correction and the dependence on T_s can be found in the analysis of the GHIGLS data in [Martin et al. \(2015\)](#).

Whether there is a significant effect on the estimated optical depth correction for the DHIGLS data would depend on whether the bright spatial structures are still unresolved at the resolution of the DRAO ST. There is the further uncertainty in the correction because the value of

T_s is not known precisely and is unlikely to be constant.

E. URSA REVISITED

For the LVC gas in the DHIGLS UM region we found a power law exponent -2.89 ± 0.04 for the N_{HI} map (Section 7.1) and -3.03 ± 0.09 for the centroid velocity map (Section 7.4).

In their analysis of LVC gas in early DRAO ST data of two adjacent intermediate-latitude pointings in Ursa Major (URSA; these correspond to the FP2 and NN pointings among our current 16 pointings for the UM-i mosaic), [Miville-Deschênes et al. \(2003a\)](#) found an exponent -3.6 ± 0.2 for both the N_{HI} map and centroid velocity map. Particular features in their data processing and analysis of the N_{HI} map might have contributed to the difference with respect to our value. (i) To mitigate against the effects of noise, the DRAO ST data were filtered. Filtering on small angular scales (high k) might remove not only noise but also some H I signal power at these k values, artificially steepening the power spectrum. (ii) No explicit allowance was made for the effect of the synthesized beam and this was stated to contribute to the reported uncertainty of the exponent. (iii) Their DRAO ST data were combined with zero-spacing data from the 26 m single dish at DRAO, which does not allow for the same cross calibration as done here for the GBT data (see Appendix C and Figure B.1). If the DRAO ST data calibration were low relative to the 26 m data, the power spectrum of N_{HI} would be artificially steepened.

It is additionally puzzling that the steeper power spectrum in this earlier work appeared to be corroborated by analysis of entirely independent Leiden/Dwingeloo H I data in a large enclosing field in the NCPL that extended the power spectrum to larger angular scales (smaller k); see Figures 14 and 15 in [Miville-Deschênes et al. \(2003a\)](#). That power spectrum produced from the Leiden/Dwingeloo data ranged from $k = 0.001 \text{ arcmin}^{-1}$ to about $0.018 \text{ arcmin}^{-1}$. According to Figure B.1 power should be reduced in this range, by the square of the $35/7$ beam of the 25 m Dwingeloo telescope, steepening the apparent power spectrum. However, this was not accounted for in their analysis. We explored this further using a 7° by 10° region selected from the GHIGLS NCPL field and a related large 25° by 25° field from LAB data. We made N_{HI} maps selecting LVC in the velocity range observed by [Miville-Deschênes et al. \(2003a\)](#) ($-6.6 < v < 19.4 \text{ km s}^{-1}$). Accounting for the respective beams, we find power spectra of N_{HI} with $\gamma = -2.68 \pm 0.14$ and -2.68 ± 0.24 for GHIGLS and LAB, respectively, consistent with what we found for the DHIGLS UM region. The results for the analysis of the corresponding centroid velocity maps are similar: $\gamma = -2.54 \pm 0.08$ and -2.42 ± 0.10 for GHIGLS and LAB, respectively. If the correction for the beam is ignored in the power spectrum model, it is clear that the fit will result in a steeper power law unless the upper limit of the fitted k -range is reduced appropriately. Note also that for the combined LAB survey, the effective beam of $40'$ and 0.5 beam sampling result in a further reduction in power at high k (see Appendix A in [Higgs et al. 2005](#)), exacerbating the steepening.

Concerns related to (i) and (ii) above would apply to the power spectrum analysis of the centroid velocity map

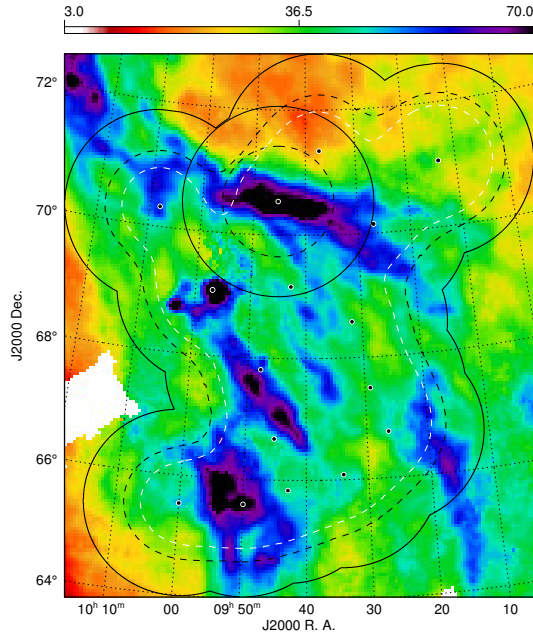


Figure F.1. Same as Figure 3, but for 16 pointings making up the mosaic of the UM region, with the highlighted NN pointing at ($9^{\text{h}}45^{\text{m}}21^{\text{s}}$, $70^{\circ}32'11''$).

and the velocity channel analysis in Miville-Deschênes et al. (2003a). For the latter, the S/N first increases as additional channels are added to the emission being integrated and the relative noise is reduced. Not accounting for this decrease in the relative noise level (for example by not including a model of the noise in the power spectrum model) could result in an artificial steepening of the power law as the noise is reduced, depending on the range in k over which the noise dominates.

F. DATA AND ANALYSIS FOR ADDITIONAL DHIGLS REGIONS

As summarized in Table 1, the DHIGLS data also include three other mosaics with fewer pointings and two single pointing syntheses. These have been processed as described for the DF-i and EN-i mosaics. An overview for each is provided in the following subsections. Note the different angular scales and the different ranges for the colorbars in the figures below.

F.1. The UM Region

The separation in the irregular grid of pointing centers (Figure F.1) for the UM-i mosaic in the GHIGLS UMA field is somewhat smaller than the FWHM of the DRAO ST primary beam. The upper panel of Figure F.2 shows the resulting noise map of UM-i. The coverage is relatively sparse compared to EN-i and DF-i, and so the noise level is higher, though at 2 K is still lower than at the centre of a single synthesis. This is slightly better than achieved in the CGPS, but the signal in this region is of course much lower than in the Galactic plane. An example signal channel from the UM-i mosaic is shown in the lower panel of Figure F.2.

The N_{HI} maps produced from the UM data cube are shown in Figure F.3, assuming $T_{\text{s}} = 80$ K. The corresponding centroid velocity maps (Section 7.4) are shown

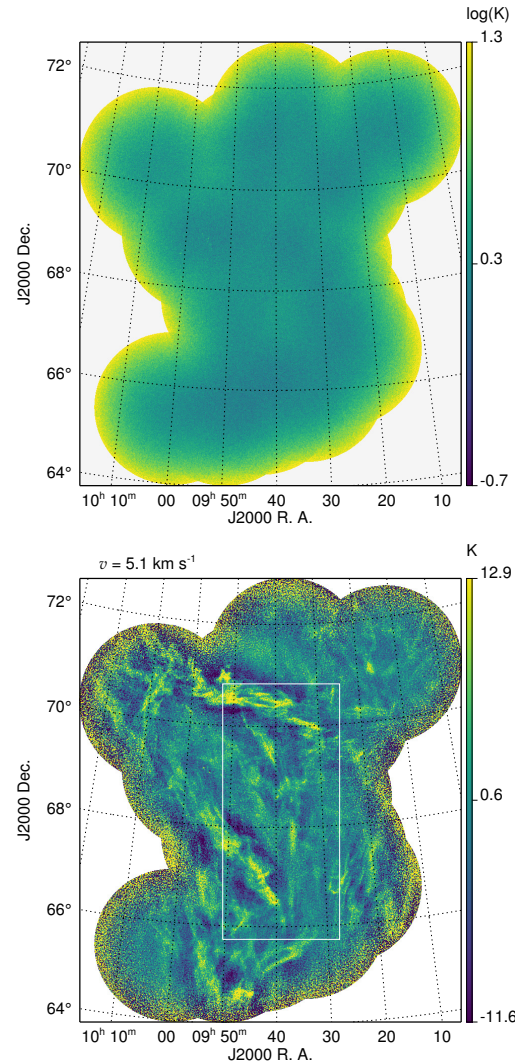


Figure F.2. Upper: Noise map for UM-i mosaic as in Figure 7. Lower: Representative channel map ($v = 5.1 \text{ km s}^{-1}$) for UM-i mosaic as in Figure 9. White rectangle indicates region used for power spectrum analysis in Figure 12.

in Figure F.4. The power spectra are discussed in Section 7.1 using data within the white dashed contour in Figure F.1.

Color maps made from the DHIGLS cube are presented in the lower panels of Figures 24 and 25. Narrow emission and absorption lines in both LVC and IVC gas are discussed in Section 8.

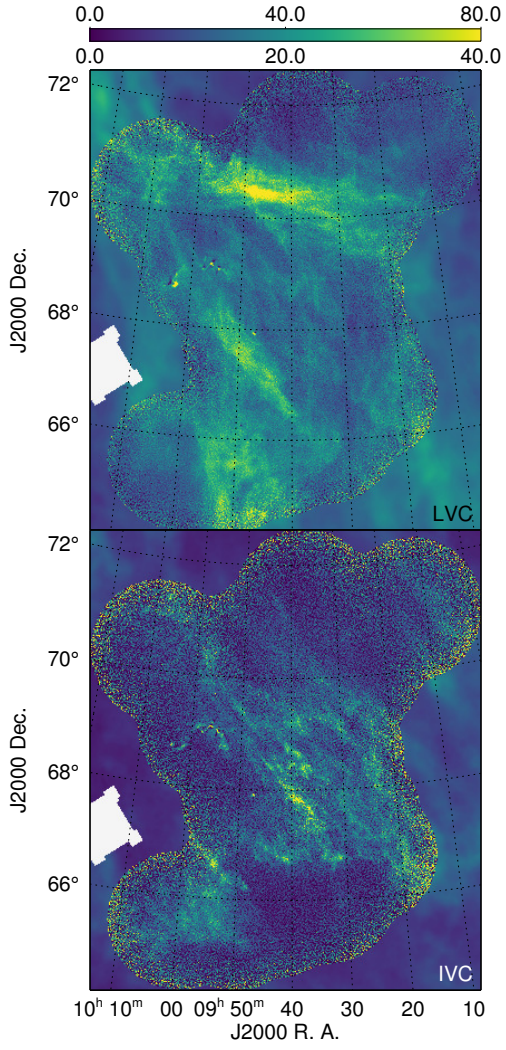


Figure F.3. Maps of N_{HI} for VCs in UM in units 10^{19} cm^{-2} for the velocity ranges in Table 2. Upper: LVC. Lower: IVC. Areas not covered by the GHIGLS NCPL combined field are white.

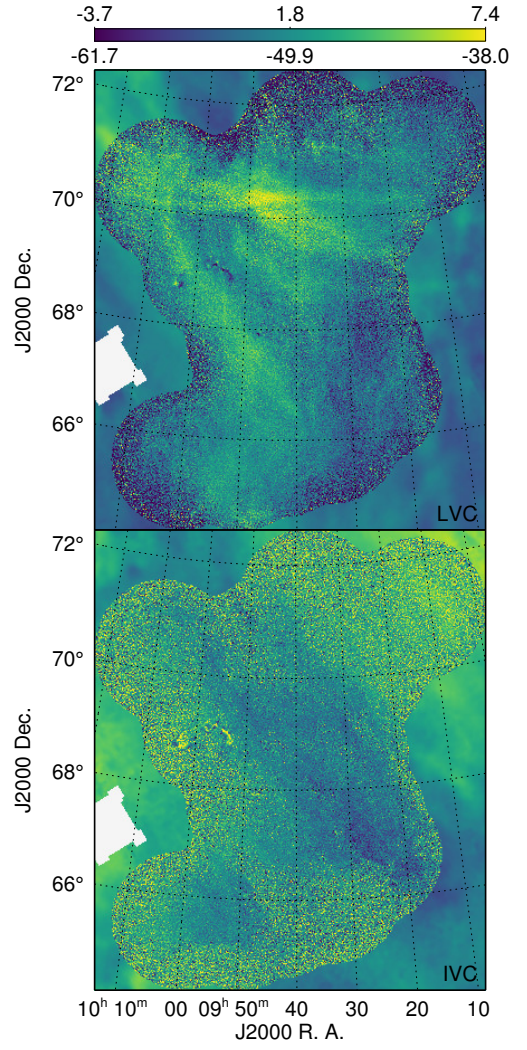


Figure F.4. Centroid velocity maps for UM LVC (upper) and IVC (lower) VCs. Units are km s^{-1} .

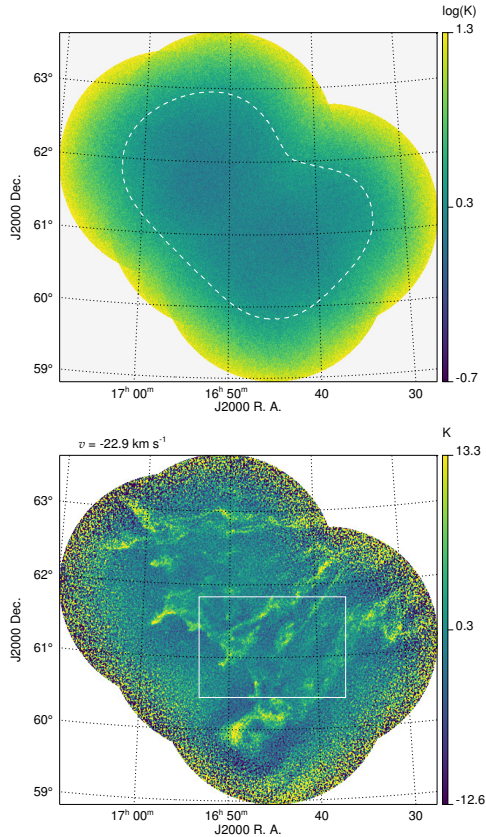


Figure F.5. Noise map and single channel map ($v = -22.9 \text{ km s}^{-1}$) for DR-i mosaic as in Figures 7 and 9. White rectangle region used for analysis of the single-channel power spectrum in Figure 12 and white dashed contour used for analysis of the VCs in Figure F.7.

F.2. The DR Region

The five pointing centers for the DR-i mosaic in the GHIGLS DRACO field can be seen in Figure 1 and the noise map for DR-i is given in Figure F.5. The minimum noise level, 1.5 K, is only slightly better than at the center of a single synthesis, reflecting the relatively sparse coverage. Also given in Figure F.5 is a channel map from DR-i representative of IVC gas with significant H I signal.

The strong IVC emission that defines the Draco nebula can also be seen in the N_{HI} map in the lower part of Figure F.6. For data within the white dashed contour, the power law exponent is -2.68 ± 0.07 (Figure F.7). For comparison, the exponent evaluated for the smaller rectangular region is -2.57 ± 0.18 and that for the single channel of DR-i analyzed in Section 4.4 is -2.27 ± 0.14 (Figure 12). On the other hand the LVC is very weak and so the exponent is less well determined: -2.87 ± 0.24 .

A color map made from the DHIGLS cube in the IVC range is presented in Figure 26. Narrow emission and absorption lines in the IVC gas are discussed in Section 8.

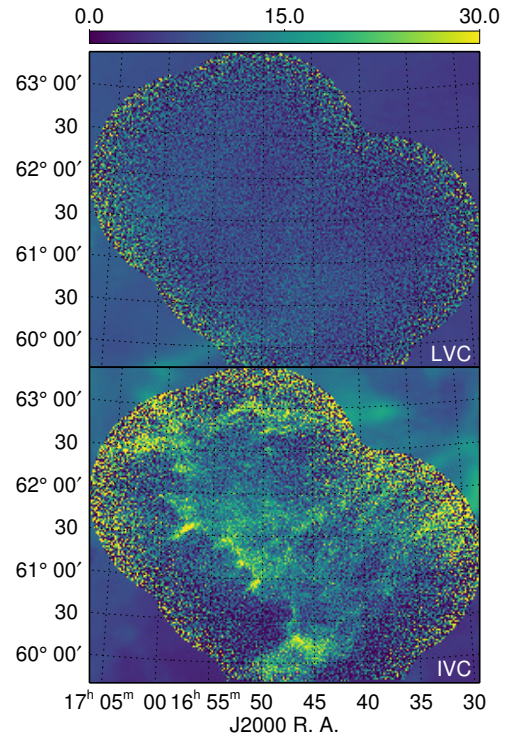


Figure F.6. Maps of N_{HI} for VCs in DR in units 10^{19} cm^{-2} for the velocity ranges in Table 2. Upper: LVC. Lower: IVC.

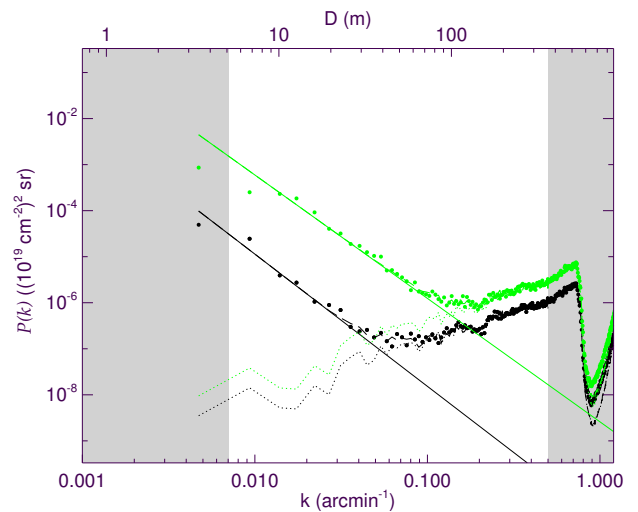


Figure F.7. As in Figure 22, for power spectra of two DR VCs: LVC (black) and IVC (green).

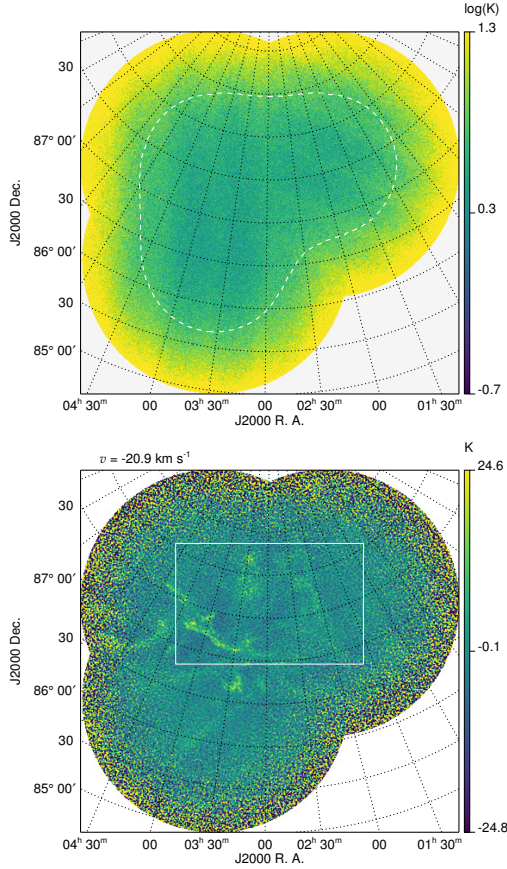


Figure F.8. Similar to Figure F.5, for PO-i mosaic. White rectangle region used for analysis of the single-channel power spectrum in Figure 12 and white dashed contour used for analysis of the VCs in Figure F.10.

F.3. The PO Region

The three pointing centers for the PO-i mosaic in the GHIGLS POL field can be seen in Figure 1 and the noise map of PO-i is given in Figure F.8. The noise level is similar to that at the center of a single synthesis (Figure 2). The lower panel of Figure F.8 shows a representative channel map of PO-i in the IVC range.

The N_{HI} maps produced from the PO data cube follow in Figure F.9. The power law exponent for the IVC data within the white dashed contour is -2.82 ± 0.08 (Figure F.10). For comparison, the exponent evaluated for the smaller rectangular region is -2.80 ± 0.15 and that for the single channel of PO-i analyzed in Section 4.4 is -2.4 ± 0.2 (Figure 12). The LVC power spectrum has a somewhat small amplitude and a similar exponent: -3.17 ± 0.16 .

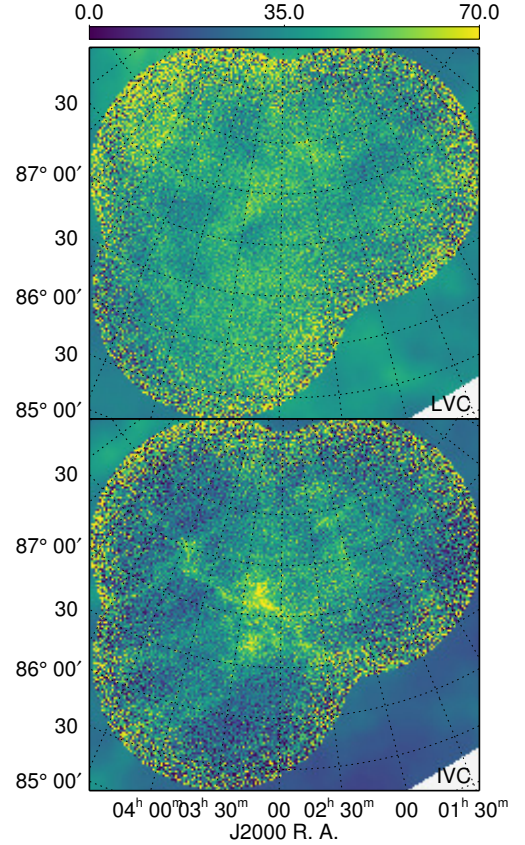


Figure F.9. Maps of N_{HI} for VCs in PO in units 10^{19} cm^{-2} for the velocity ranges in Table 2. Upper: LVC. Lower: IVC.

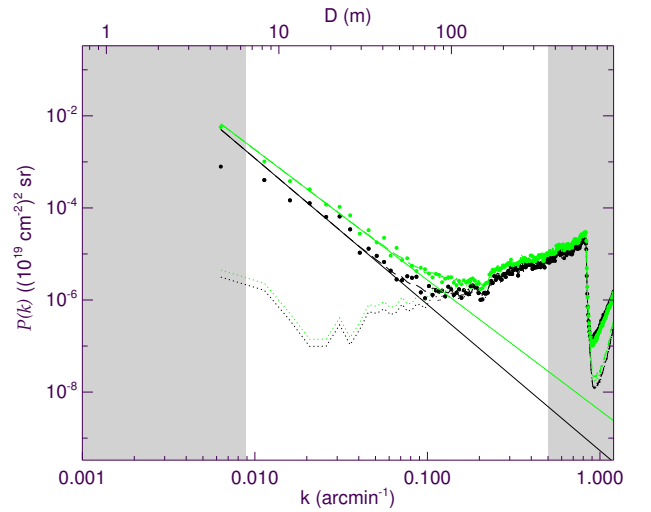


Figure F.10. As in Figure 22, for power spectra of two PO VCs: LVC (black) and IVC (green).

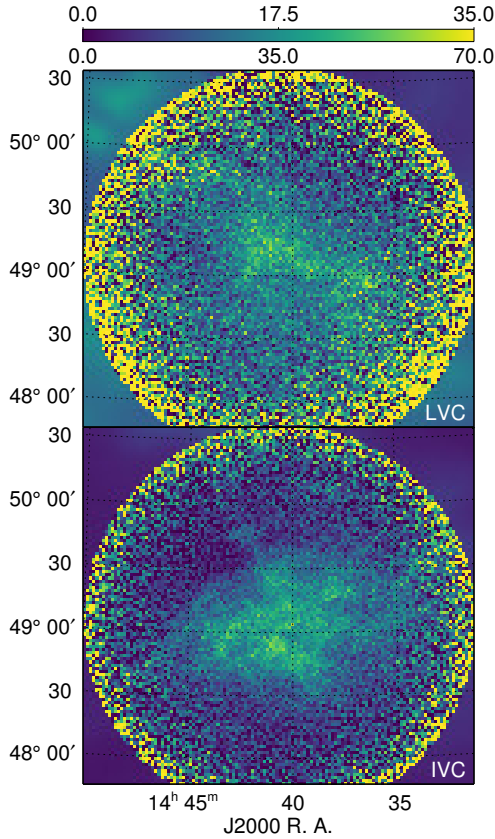


Figure F.11. N_{HI} component maps from single-synthesis region MG within GHIGLS field G86, for the velocity ranges in Table 2. Upper: LVC. Lower: IVC. Units are 10^{19} cm^{-2} .

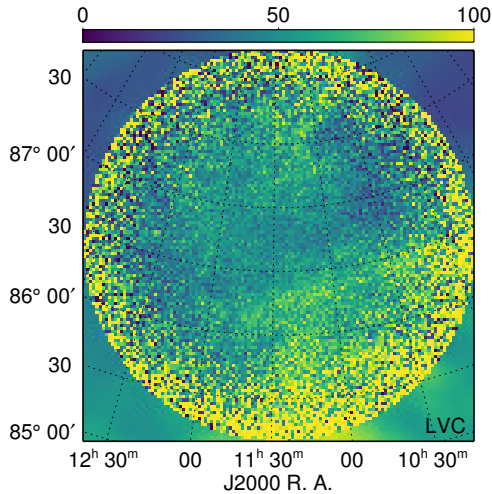


Figure F.12. N_{HI} map of single-synthesis region MC within GHIGLS field POL, for the LVC velocity range in Table 2. Units are 10^{19} cm^{-2} .

F.4. Single Syntheses MG in G86 and MC in POL

The noise maps for the two single syntheses, MG in the GHIGLS G86 field and MC in the GHIGLS POL field, are like that shown for DF20 in Figure 2, with slightly different values of $\sin \delta$.

In Figure F.11, it can be seen that compared to the LVC in MG, the IVC has a higher column density and

more spatial structure. The N_{HI} map for LVC in MC follows in Figure F.12 (IVC is much less significant).

F.5. Other Data from the DRAO ST

In this paper we are focusing on the mosaics from H I spectral-line data. However, we note that, as was the case for the CGPS, survey products derived from observations using the DRAO ST also include complementary continuum mosaics at 408 MHz and 1420 MHz and polarization mosaics in four bands near 1420 MHz. Such data enable many studies (Kotthes et al. 2010). Point source catalogs can be constructed with flux density, spectral index, and polarization information. The polarization properties of radio galaxies have been analyzed using the deepest continuum data then available, in EN (Taylor et al. 2007; Grant et al. 2010). Rotation measures of point sources can be used to probe the magnetic field (Brown et al. 2003), in this case at higher latitude including the Galactic halo (Mao et al. 2012). Diffuse emission at 408 MHz and at 1420 MHz in polarization can be mapped (Landecker et al. 2010), now at intermediate latitude. The potential correlation with H I structures can also be explored, but all of these studies are beyond the scope of this paper.

REFERENCES

- Barriault, L., Joncas, G., Falgarone, E., et al. 2010, MNRAS, 406, 2713
- Bertincourt, B., Lagache, G., Martin, P. G., et al. 2016, A&A, 588, A107
- Beuther, H., Bihr, S., Rugel, M., et al. 2016, ArXiv e-prints, arXiv:1609.03329
- Boothroyd, A. I., Blagrave, K., Lockman, F. J., et al. 2011, A&A, 536, A81
- Brown, J. C., Taylor, A. R., & Jackel, B. J. 2003, ApJS, 145, 213
- Bryan, G. L., Norman, M. L., O’Shea, B. W., et al. 2014, ApJS, 211, 19
- Calabretta, M. R., & Greisen, E. W. 2002, A&A, 395, 1077
- Chandrasekhar, S. 1949, ApJ, 110, 329
- Condon, J. J., Cotton, W. D., Greisen, E. W., et al. 1998, AJ, 115, 1693
- Cox, D. P. 2005, ARA&A, 43, 337
- Deshpande, A. A., Dwarakanath, K. S., & Goss, W. M. 2000, ApJ, 543, 227
- Dewdney, P. E., Higgs, L. A., & Knee, L. B. G. 2002, in Proceedings of the XXVIIth General Assembly of the International Union of Radio Science, 17-24 August, Maastricht, the Netherlands. Online at <http://www.ursi.org/Proceedings/ProcGA02/papers/p2117.pdf>, 1
- Dickey, J. M., McClure-Griffiths, N. M., Stanimirović, S., Gaensler, B. M., & Green, A. J. 2001, ApJ, 561, 264
- Dobbs, C. L., Krumholz, M. R., Ballesteros-Paredes, J., et al. 2014, Protostars and Planets VI, 3
- Gillmon, K., Shull, J. M., Tumlinson, J., & Danforth, C. 2006, ApJ, 636, 891
- Gladders, M. D., Clarke, T. E., Burns, C. R., et al. 1998, ApJ, 507, L161
- Goerigk, W., Mebold, U., Reif, K., Kalberla, P. M. W., & Velden, L. 1983, A&A, 120, 63
- Grant, J. K., Taylor, A. R., Stil, J. M., et al. 2010, ApJ, 714, 1689
- Green, D. A. 1993, MNRAS, 262, 327
- Green, D. A. 2007, in IAU Symposium, Vol. 237, IAU Symposium, ed. B. G. Elmegreen & J. Palous, 413
- Heitsch, F., & Putman, M. E. 2009, ApJ, 698, 1485
- Hennebelle, P., & Falgarone, E. 2012, A&A Rev., 20, 55
- Hennebelle, P., & Iffrig, O. 2014, A&A, 570, A81
- Herbstmeier, U., Heithausen, A., & Mebold, U. 1993, A&A, 272, 514

- Higgs, L. A., Hoffmann, A. P., & Willis, A. G. 1997, in *Astronomical Society of the Pacific Conference Series*, Vol. 125, *Astronomical Data Analysis Software and Systems VI*, ed. G. Hunt & H. Payne, 58
- Higgs, L. A., Landecker, T. L., Asgekar, A., et al. 2005, *AJ*, 129, 2750
- Higgs, L. A., & Tapping, K. F. 2000, *AJ*, 120, 2471
- Joncas, G., Boulanger, F., & Dewdney, P. E. 1992, *ApJ*, 397, 165
- Kalberla, P. M. W. 2003, *ApJ*, 588, 805
- Kalberla, P. M. W., Burton, W. B., Hartmann, D., et al. 2005, *A&A*, 440, 775
- Kalberla, P. M. W., & Haud, U. 2015, *A&A*, 578, A78
- Kim, C.-G., & Ostriker, E. C. 2015, *ApJ*, 802, 99
- Kim, C.-G., Ostriker, E. C., & Kim, W.-T. 2014, *ApJ*, 786, 64
- Kothes, R., Landecker, T. L., & Gray, A. D. 2010, in *Astronomical Society of the Pacific Conference Series*, Vol. 438, *The Dynamic Interstellar Medium: A Celebration of the Canadian Galactic Plane Survey*, ed. R. Kothes, T. L. Landecker, & A. G. Willis, 415
- Landecker, T. L., Dewdney, P. E., Burgess, T. A., et al. 2000, *A&AS*, 145, 509
- Landecker, T. L., Reich, W., Reid, R. I., et al. 2010, *A&A*, 520, A80
- Lazarian, A., & Pogosyan, D. 2000, *ApJ*, 537, 720
- Lee, M.-Y., Stanimirović, S., Murray, C. E., Heiles, C., & Miller, J. 2015, *ApJ*, 809, 56
- Lonsdale, C. J., Smith, H. E., Rowan-Robinson, M., et al. 2003, *PASP*, 115, 897
- Mao, S. A., McClure-Griffiths, N. M., Gaensler, B. M., et al. 2012, *ApJ*, 755, 21
- Markwardt, C. B. 2009, in *Astronomical Society of the Pacific Conference Series*, Vol. 411, *Astronomical Data Analysis Software and Systems XVIII*, ed. D. A. Bohlender, D. Durand, & P. Dowler, 251
- Martin, P. G., Blagrove, K. P. M., Lockman, F. J., et al. 2015, *ApJ*, 809, 153
- Martin, P. G., Rogers, C., Reach, W. T., Dewdney, P. E., & Heiles, C. E. 1994, in *Astronomical Society of the Pacific Conference Series*, Vol. 58, *The First Symposium on the Infrared Cirrus and Diffuse Interstellar Clouds*, ed. R. M. Cutri & W. B. Latter, 188
- McClure-Griffiths, N. M., Dickey, J. M., Gaensler, B. M., et al. 2005, *ApJS*, 158, 178
- Meyerdierks, H., Heithausen, A., & Reif, K. 1991, *A&A*, 245, 247
- Miville-Deschênes, M.-A., Joncas, G., Falgarone, E., & Boulanger, F. 2003a, *A&A*, 411, 109
- Miville-Deschênes, M.-A., Lagache, G., Boulanger, F., & Puget, J.-L. 2007, *A&A*, 469, 595
- Miville-Deschênes, M.-A., Lagache, G., & Puget, J.-L. 2002, *A&A*, 393, 749
- Miville-Deschênes, M.-A., Levrier, F., & Falgarone, E. 2003b, *ApJ*, 593, 831
- Miville-Deschênes, M.-A., & Martin, P. G. 2007, *A&A*, 469, 189
- Miville-Deschênes, M.-A., Martin, P. G., Abergel, A., et al. 2010, *A&A*, 518, L104
- Miville-Deschênes, M.-A., Salomé, Q., Martin, P. G., et al. 2016, *ArXiv e-prints*, arXiv:1602.03340
- Murray, C. E., Stanimirović, S., Goss, W. M., et al. 2015, *ApJ*, 804, 89
- Oliver, S. J., Bock, J., Altieri, B., et al. 2012, *MNRAS*, 424, 1614
- Pidopryhora, Y., Lockman, F. J., Dickey, J. M., & Rupen, M. P. 2015, *ApJS*, 219, 16
- Planck Collaboration XXIV. 2011, *A&A*, 536, A24
- Planck Collaboration XI. 2014, *A&A*, 571, A11
- Planck Collaboration XIII. 2014, *A&A*, 571, A13
- Planck Collaboration Int. XVII. 2014, *A&A*, 566, A55
- Prestage, R. M., Constantikes, K. T., Hunter, T. R., et al. 2009, *IEEE Proceedings*, 97, 1382
- Rachford, B. L., Snow, T. P., Destree, J. D., et al. 2009, *ApJS*, 180, 125
- Roy, N., Kanekar, N., & Chengalur, J. N. 2013, *MNRAS*, 436, 2366
- Sault, R. J., & Killeen, N. 2011, ftp://ftp.atnf.csiro.au/pub/software/miriad/userguide_US.ps.bz2, 193
- Sault, R. J., Teuben, P. J., & Wright, M. C. H. 1995, in *Astronomical Society of the Pacific Conference Series*, Vol. 77, *Astronomical Data Analysis Software and Systems IV*, ed. R. A. Shaw, H. E. Payne, & J. J. E. Hayes, 433
- Saury, E., Miville-Deschênes, M.-A., Hennebelle, P., Audit, E., & Schmidt, W. 2014, *A&A*, 567, A16
- Schneider, E. E., & Robertson, B. E. 2015, *ApJS*, 217, 24
- Stanimirovic, S. 1999, PhD thesis, Univ. Western Sydney, Nepean
- Stanimirovic, S. 2002, in *Astronomical Society of the Pacific Conference Series*, Vol. 278, *Single-Dish Radio Astronomy: Techniques and Applications*, ed. S. Stanimirovic, D. Altschuler, P. Goldsmith, & C. Salter, 375–396
- Sternberg, A., Le Petit, F., Roueff, E., & Le Bourlot, J. 2014, *ApJ*, 790, 10
- Stil, J. M., Taylor, A. R., Dickey, J. M., et al. 2006, *AJ*, 132, 1158
- Taylor, A. R., Gibson, S. J., Peracaula, M., et al. 2003, *AJ*, 125, 3145
- Taylor, A. R., Stil, J. M., Grant, J. K., et al. 2007, *ApJ*, 666, 201
- Thom, C., Peek, J. E. G., Putman, M. E., et al. 2008, *ApJ*, 684, 364
- Valdivia, V., Hennebelle, P., Gérin, M., & Lesaffre, P. 2016, *A&A*, 587, A76
- Wakker, B. P. 2006, *ApJS*, 163, 282
- Willis, A. G. 1999, *A&AS*, 136, 603
- Winkel, B., Kerp, J., Flöer, L., et al. 2016, *A&A*, 585, A41
- Wolfire, M. G. 2015, *Highlights of Astronomy*, 16, 600
- Wolfire, M. G., McKee, C. F., Hollenbach, D., & Tielens, A. G. G. M. 2003, *ApJ*, 587, 278